

CONFERENCES AND SYMPOSIA

PACS number: 01.10.Fv

Scientific session of the Physical Sciences Division of the Russian Academy of Sciences (31 January 2007)

A scientific session of the Physical Sciences Division of the Russian Academy of Sciences (RAS) was held in the Conference Hall of the P N Lebedev Physical Institute, RAS on 31 January 2007. The following reports were presented at the session:

(1) **Koshelev K N** (Institute of Spectroscopy, RAS, Troitsk, Moscow region), **Banine V E** (ASML, Veldhoven, the Netherlands), **Salashchenko N N** (Institute for the Physics of Microstructures, RAS, Nizhny Novgorod). "Research and development in short-wave radiation sources for new-generation lithography";

(2) **Balykin V I** (Institute of Spectroscopy, RAS, Troitsk, Moscow region). "Parallel fabrication of nanostructures via atom projection";

(3) **Lozovik Yu E, Popov A M** (Institute of Spectroscopy, RAS, Troitsk, Moscow region). "Properties and nanotechnological applications of nanotubes".

An abridge version of the reports is given below.

PACS numbers: **42.72.–g**, 42.82.Cr
DOI: 10.1070/PU2007v050n07ABEH006321

Research and development in short-wave radiation sources for new-generation lithography

K N Koshelev, V E Banine, N N Salashchenko

In the impressive list of scientific, technical, and technological problems that lie ahead in the realization of short-wavelength lithography, the radiation source is far from last in terms of complexity of the problems encountered. A wavelength of 13.5 nm for new-generation lithography — extreme ultraviolet (EUV) lithography — had been accepted long before it became more or less clear how the source might be arranged to afford commercially expedient production — high volume manufacturing (HVM). The choice was made partly proceeding from the nature of fabrication and properties of multilayer mirrors and partly in the belief that the function of emitters would most likely be fulfilled by the Ly_α line of hydrogenlike Li^{+2} ions (13.5 nm) or the emission peak arising from radiative transitions in the Xe^{+9} ion.

The plasma radiating in the far vacuum ultraviolet (VUV) range has been long and much studied. However, the technical requirements imposed on an HVM source are so extraordinary that the seemingly simple task of heating the plasma to a temperature of several dozen electron-volts transforms into a whole set of challenging physical, engineering, and technical problems. We will consider these requirements in greater detail. In lithography, it is the practice to characterize the source by the radiation power at the so-called 'intermediate focus' (IF) at the output of the primary radiation collection system (Fig. 1).

One consequence of using the sophisticated optics of a lithographic apparatus with a large number (up to 11) of reflecting multilayer mirror surfaces is that only a narrow radiation band with a width of 2% centered at 13.5 nm may be employed to print microcircuits. The minimal required radiation power at the IF reaches 180 W. When the efficiency of the primary radiation collection (the solid angle of collection and the reflectivities) and the inevitable losses in the devices which shield the optics from 'contamination' are accounted for, one is led to the following estimate of the output source power: the average 'useful' power of radiation into a solid angle of 2π and a narrow 2% bandwidth should be no less than 2000 W. It is conventional to characterize the source by the electric energy-to-'useful' radiation conversion efficiency (CE). The effective size of the emitting volume should not exceed 1 mm^3; the source operating frequency is about 10 kHz, and the stability of the radiation dose is $3\sigma \leqslant 0.3\,\%$ (in 50 shots).

Lithium as the working material was rejected at a rather early stage of research, primarily due to extraordinary technological problems and the hazard of contamination of the entire lithography system by a chemically highly deleterious element. Experiments with the more convenient, chemically neutral xenon showed that the CE amounts to only 0.5 – 0.7% for a pulsed discharge plasma. This signifies that the average electric power released in the small source volume should be as high as 300 – 400 kW.

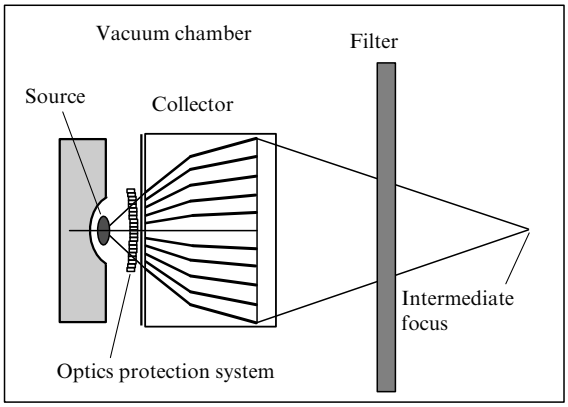

Figure 1. Defining the parameters of an EUV lithography source.

Uspekhi Fizicheskikh Nauk **177** (7) 777 – 799 (2007)
Translated by E N Ragozin; edited by A Radzig

The estimates given above apply to a discharge plasma-based source. Another possible candidate is a laser-produced plasma (LPP). The LPP as an EUV source offers several advantages over discharge plasmas. These include a somewhat higher CE, higher radiation collection efficiency, and what may be a simpler system of optics protection from the destructive effect of corpuscular radiation. However, the most significant and perhaps decisive argument for the source selection is the high cost of laser systems with an average output power of many dozens of kilowatts. Clearly, this argument is temporal in nature, since the commercial price of any hi-tech product tends to steadily decline. However, present-day plans of the main manufacturers of lithography apparatus place an emphasis on the use of discharge plasma-based EUV sources. Below, we will describe several results in the development of discharge sources and in so doing rely primarily on the collaboration of the Institute of Spectroscopy, Russian Academy of Sciences, with the leading manufacturer of lithography apparatus, ASML (the Netherlands), under the integrated project MoreMoore of the 6th Framework Program of the European Community.

The low efficiency of xenon stems, in particular, from the fact that only several lines of an Xe^{+9} ion radiate in the narrow spectral range employed. As a result, the useful radiation in nonstationary and nonuniform plasmas of pulsed discharges and laser jets occurs for a substantially shorter time than the total duration of the high-temperature phase, and by no means does the total volume of the temperature-nonuniform plasma emit useful photons. A possible solution to this seemingly insurmountable problem was prompted by atomic physics — using the radiation of multiply charged tin ions.

From the viewpoint of basic atomic spectroscopy there are several arguments in favor of acceptance of tin as the working material for the radiation source at a wavelength of 13.5 nm. The resonance transitions in $Sn^{+8}-Sn^{+13}$ ions are $4d^k-(4d^{k-1}4f+4p^54d^{k+1})$ transitions. The strong 4d–4f exchange interaction in the $4d^{k-1}4f$ configuration and 4p–4d exchange interaction in the $4p^54d^{k+1}$ configuration have the effect that the energy levels of these configurations split into two bands, with the probabilities of transitions from the upper band being much higher than those from the lower band. The strong interaction between the $4d^{k-1}4f$ and $4p^54d^{k+1}$ configurations makes this band narrowing still stronger. As a result, the emission concentrates in a narrow spectral interval despite the presence of several hundred levels within a broad energy interval. Furthermore, owing to a weak dependence of the excitation energy in $n=4-n'=4$ transitions on the ion multiplicity, intense transitions in several neighboring ions fall into this interval. A comprehensive study of the tin plasma spectrum excited in a vacuum spark was pioneered by research on the EUV lithography source [2].

Even the first experiments with a discharge in tin vapor revealed a substantial rise in CE — from 0.5–0.7% to 2% or even 3%. The requirements for the power released in the discharge were considerably relaxed, but the requisite power was still equal to about 100 kW — a quantity too great for a single source of small size. Prior to formulating the approaches that permit operation in the mode of extreme thermal load, we address ourselves to the physics of the discharge employed. For a plasma source we selected a classical vacuum spark, i.e., a discharge between two electrodes, with the working material being fed to the interelectrode gap by way of cathode material (tin) ablation using laser radiation pulses. Research into axially symmetric discharges, and, in particular, vacuum sparks, showed that soft X-ray and VUV radiation is excited in plasmas with currents exceeding 10 kA at the moment the sausage type instability develops in the discharge column. It is known that these constrictions, or 'micropinches', are produced due to plasma outflow under conditions of great radiation losses, due to the line emission of multiply charged tin ions in this case (see, for instance, Ref. [3]). The plasma outflow from a pinch is accompanied by plasma compression, heating, and passage to progressively higher ionization stages. The pinch radius is defined by the balance between Joule heating and energy loss, primarily radiation loss in optically dense plasma.

The process continues until either the radiation loss ceases to compensate for the Joule heat release or anomalous resistance develops in the plasma due to the small number of current carriers. At this stage, a rapid plasma expansion and a micropinch decay occur. The instability development may be illustrated with the aid of a diagram (Fig. 2) which shows the pinch radius as a function of the total number of ions in the discharge cross section (the linear ion density N_i). The direction of development trajectory — the lowering of the linear density — is indicated by an arrow. At each instant of time, slowly contracting pinches satisfy (or almost satisfy) the thermal–magnetic pressure equilibrium condition, viz. the Bennett relation

$$N_i(Z+1)\,T\sim I^2\,,$$

so that each point of the trajectory in Fig. 2 can be related to the plasma temperature rising along the trajectory. For fast, dynamic pinches, departures from the Bennett relation may be significant.

For currents $I\approx 10-30$ kA, the temperature $T\approx 20-40$ eV is reached when a plasma column is compressed to lateral dimensions of about 200 μm. The constrictions (micropinches) observed in the discharge column of the vacuum spark are exemplified in Fig. 3.

Several EUV-emitting micropinches are observed to occur (quite often sequentially in time). This phenomenon of radiative domain 'zippering' along the discharge axis determines the time-integrated axial source dimension.

This brings up a curious question: How can one hope for dose stability of the EUV radiation excited in the discharge in

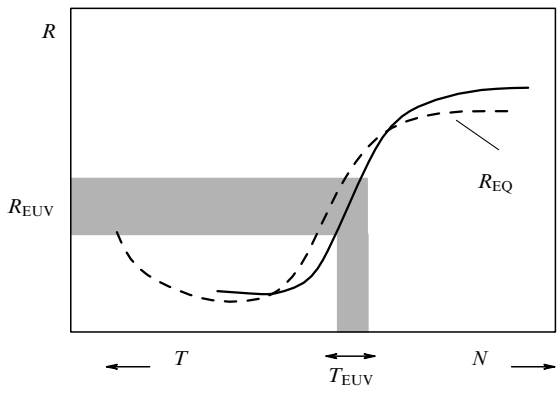

Figure 2. Equilibrium radius of the Bennett pinch (dashed line). The temperature T_{EUV} required for the excitation of EUV photons corresponds to constriction to a radius R_{EUV}.

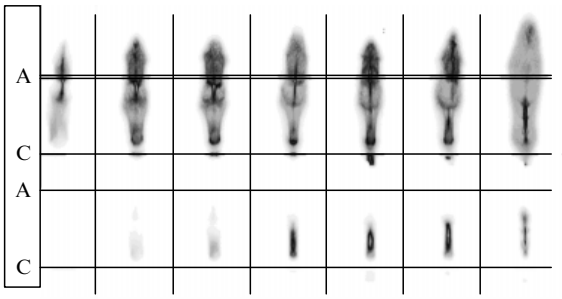

Figure 3. Images of the plasma column recorded in the intrinsic short-wave plasma radiation using a time-gated microchannel plate (MCP) detector adjustable from 3 to 50 ns. Images in the upper part of the picture correspond to radiation in the entire MCP sensitivity range (< 100 nm); the images in the lower part were produced via a Zr/Si filter. The distance between the anode A and the cathode C is 3 mm.

the course of instability development — in this case, the sausage type instability well known in plasma physics? The more so as we are dealing with a vacuum spark — a discharge with rather unstable initial parameters, first and foremost with the poorly reproducible initial distribution of the working material in the interelectrode gap. It turned out, however, that there is such a domain of parameters (the initial radius and the total amount of vaporized material) for which the instability development trajectory depends only slightly on them [4]. This circumstance is illustrated in Fig. 4a. This fact is amply borne out by experiments with an EUV source:

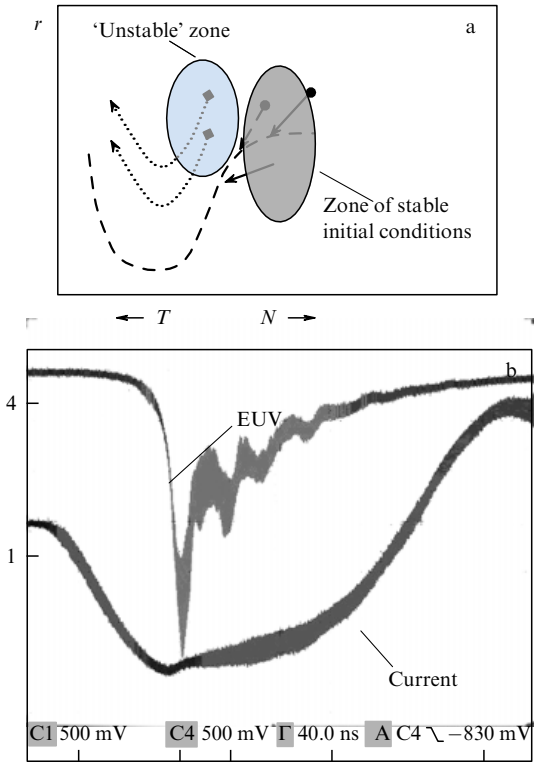

Figure 4. (a) Stable (dashed curve) and unstable (dotted curves) micropinch development trajectories in the coordinates of the pinch radius r and the linear particle density N. (b) Superimposed oscilloscope traces of the current and the EUV radiation from 256 laser-triggered vacuum spark discharges with a peak current of about 10 kA.

Fig. 4b depicts superimposed (and well coincident) oscilloscope traces of the current and the EUV radiation from 256 laser-triggered vacuum spark discharges with a peak current of about 10 kA.

The changeover to a tin plasma as an EUV radiator with a CE as high as 2 – 3% permits relaxing the requirements for the electric power liberated in the discharge down to 100 kW. For a discharge with a size of several millimeters this still remains an inconceivably high value. A possible solution involves the so-called source 'multiplication', i.e., production of a multitude of radiation sources, so as to distribute the electric and thermal load among them. However, the requirement that the radiator be fixed in space and the high repetition rate (up to 10 kHz) are practically incompatible with a 'revolver' system with a mechanical reiteration of a large number of vacuum sparks having axially symmetric systems of electrodes and insulators. This is precisely the reason why the multiplication of a xenon source appeared to be practically infeasible.

The use of tin in combination with a laser initiation opens up new possibilities. Feeding the material to the interelectrode gap by vaporizing the electrode surface under pulsed laser irradiation ensures the initial axial symmetry irrespective of the electrode shapes: the initial plasma expands as a cone with its axis perpendicular to the electrode surface. One version of the system with revolving electrodes, the lower of which is covered with liquid tin (for ease of surface recovering), is schematically depicted in Fig. 5.

When the electrodes rotate, tin is vaporized from a new segment of the cathode ring with each new laser shot, the focal position remaining invariable. This therefore gives rise to a sequence of elementary vacuum sparks in the same point in space, which nevertheless pertain to different segments of the plane electrodes — the cathode and the anode. It is only desirable that the previous position of the laser focal spot should shift relative to the next one by a distance of 1 – 2 mm (the size of the surface zone temporarily 'spoiled' by the discharge) during the time interval between the pulses. For a repetition rate of 10^4 Hz this corresponds to the lowest admissible linear rotation velocity on the order of 10 m s^{-1}. Experiments and calculations show that these systems are capable of withstanding electrical power as high as 50 kW, and maybe 100 kW.

The idea of 'continuous multiplication' was further developed in the jet version of the EUV source. It has been suggested that two liquid jets of a metal or an alloy with a moderate melting temperature flowing out of metal nozzles at a high velocity should be used as the electrodes. Pumps maintain a liquid metal pressure in the system at several dozen atmospheres to make the jets move at a speed of several

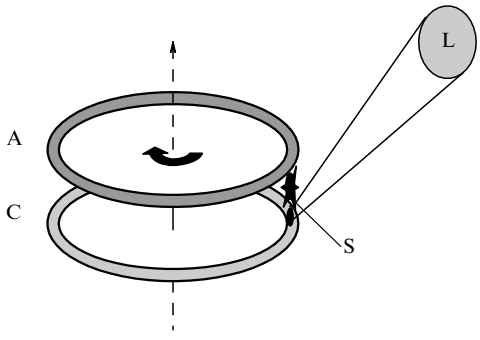

Figure 5. Schematic of the 'wheel' multiplication.

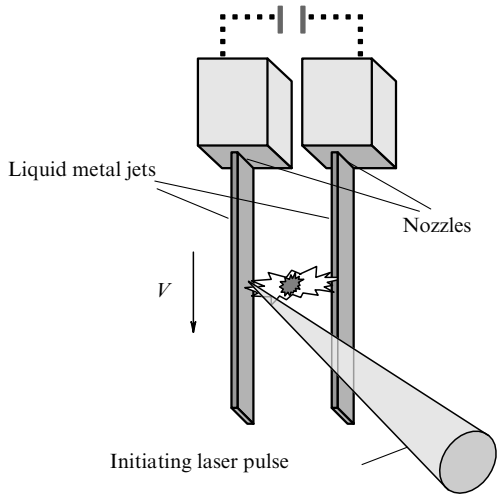

Figure 6. Schematic representation of the 'jet' EUV radiation source.

dozen meters per second, thereby ensuring nozzle cooling and the heat removal.

The voltage is applied across the jets, and the discharge between them occurs when laser radiation is focused onto one of them (Fig. 6). Not only do the jets remove the heat released in the discharge, but they also efficiently cool the metal elements closest to the discharge — the nozzles. The jets end up in the heat exchanger and return to the system after cooling with the aid of pumps. The power resource of this technical solution amounts to 200 kW.

In the foregoing, we discussed several approaches to the solutions of two problems — increasing the radiation power (the thermal load), and improving the radiation dose stability. Lying outside of the scope of our report were such important aspects of lithographic apparatus development as the lifetimes of the electrodes and optical elements, primarily, the radiation collector. The latter problem is directly related to the physics of the radiation source, because it arises from the so-called debris — corpuscular streams (atoms, ions, droplets of electrode material) emanating from the discharge region.

The demonstration EUV lithography apparatus (the so-called alpha tool) has already been made and is familiar to the industry. However, its main parameters are lower by a factor of ten or more than the parameters complying with the HVM requirements. The industry has allowed researchers the relatively little leeway of two years to overcome this gap.

References

1. Banine V, Moors R *J. Phys. D: Appl. Phys.* **37** 3207 (2004)
2. Churilov S S, Ryabtsev A N *Phys. Scripta* **73** 614 (2006)
3. Koshelev K N, Pereira N R *J. Appl. Phys.* **69** R21 (1991)
4. Antsiferov P S et al. *J. Phys. D: Appl. Phys.* **22** 1073 (1989)
5. Koshelev K N et al., in *EUV Sources for Lithography* (Ed. V Bakshi) (Bellingham, Wash.: SPIE Press, 2006) p. 175
6. Borisov V M et al., in *EUV Sources for Lithography* (Ed. V Bakshi) (Bellingham, Wash.: SPIE Press, 2006) p. 477

PACS numbers: **81.07.–b**, **81.16.–c**, 81.16.Ta
DOI: 10.1070/PU2007v050n07ABEH006322

Parallel fabrication of nanostructures via atom projection

V I Balykin

1. Introduction

There are two radically different approaches to the development of nanotechnology. These approaches are commonly referred to as the 'top down' and 'bottom up' technologies. The top down approach involves reducing the dimensions of physical bodies to objects with nanometric parameters. For instance, semiconductor microelectronic devices are fabricated by the optical lithography technique whereby the intermediate product is processed by a laser beam and the minimal dimension of the elements of the created microelectronic circuit is defined by the laser radiation wavelength. We note that the diffraction limit of the resolution of conventional optical lithography is about 65 nm. There are several other approaches to top down technology, each of them possessing both advantages and disadvantages: charged-particle beam lithography encounters problems associated with batch production of structures and the significant part played by Coulomb repulsion; self-organizing fabrication still calls for a better understanding of the physical processes.

Bottom up technology consists in the nanoobject under fabrication being 'assembled' of individual atoms, molecules, biological cells, etc. The feasibility and promise of this approach was first pointed out by Richard Feynman in his report to the annual meeting of the American Physical Society in 1959 [1]. The practical realization of bottom up technology became possible with the development of the probe microscopy technique which enabled not only observations of nanoobjects with atomic resolution but also manipulations of single atoms and molecules. This was first accomplished by researchers at an IBM laboratory, who managed to inlay their company's name (IBM) with 35 xenon atoms on the surface of a nickel single crystal [2]. This technique opens up many possibilities for manipulations at the level of individual atoms and molecules. However, methods reliant on the employment of scanning probes are generally characterized by low productivity and high cost.

Fabricating nanostructures with a size of about 10 nm presents a complex technological problem which is important from both the practical and theoretical viewpoints, because these structures bridge the gap between the classical and quantum-mechanical worlds.

2. Atom optics and atom nanooptics

Atom optics is an alternative approach to nanotechnology based on the bottom up principle. Atom optics is the optics of material particles (along with electron, ion, and neutron optics) and it concerns with the problems of formation of the ensembles and beams of neutral atoms, control over them, and their application. The term *atom optics* is similar to the terms *light optics* or photon optics. Basically, atom optics relies on three main techniques: the first depends on atom–matter interactions, the second on the interaction between atoms having a magnetic or electric dipole moment and a static electric or magnetic field, and the third on the resonance

(or quasiresonance) interaction between an atom and an optical field.

As a result of intensive development during the last 10–15 years, atom optics has become an important part of atomic, molecular, and optical physics, making contributions to different technologies [3–10]. Among important areas of atom optics is the development of basic elements similar to the well-known elements of ordinary light optics, like atom lenses, mirrors, beam splitters, and interferometers, as well as the application of these elements in practical devices. In particular, one of the numerous applications of atom-optics elements — *atom lithography* — is of considerable interest for the micro- and nanofabrication of material structures. In atom lithography, the internal and (or) external degrees of freedom of individual atoms are controlled by external electromagnetic fields with nanometer precision, making it possible to produce structures on the surface. This method offers several advantages over other methods, because it makes use of neutral atoms. First and foremost the fundamental spatial resolution limit inherent in this method is imposed by diffraction and proves to be extremely short, because atoms have relatively large masses and accordingly short de Broglie wavelengths. Furthermore, Coulomb repulsion forces are absent when use is made of neutral atoms. Lastly, it is possible to realize manipulation of atoms in parallel, making it possible to simultaneously treat relatively large surfaces. The possibility of depositing atoms on a surface with atomic precision by atom-optics techniques was first pointed out by Balykin and Letokhov [11, 12].

We will consider below the main nanostructure fabrication techniques utilized in atom optics.

2.1 Atom fabrication of nanostructures based on traveling and standing light waves

In recent years, several proposals have been made and a series of experiments have been conducted on the nanofabrication of atomic structures by atomic beams focused with the help of traveling and standing light waves [11–26]. By and large, it is possible to indicate two main ideas of focusing atoms by the laser radiation of traveling and standing light waves. One of them is the focusing of atoms by *a single laser beam*, which was first realized with the use of a sodium atomic beam [13, 14] and a Gaussian laser beam which played the part of an atom lens. This technique was extended to other atoms and differently configured laser beams, including so-called hollow beams [11, 12, 15, 16]. Figure 1a schematically depicts the focusing of atoms on a domain measuring several angströms using the TEM_{01}^{*} laser mode. In the propagation of atoms inside a hollow laser beam there occurs their focusing under the gradient force of light pressure. The atomic density distribution (Fig. 1b) over the focal plane of this atom lens has a width on the order of one angström, i.e., it is comparable to atomic dimensions [11, 12].

Another idea of constructing nanostructures involves the focusing of atoms by a standing laser radiation wave [17–26], which is of particular interest for the fabrication of periodic submicrometer structures. The first demonstration of atomic structure deposition by a standing light wave was given with sodium atoms [17]. McClelland et al. [21] deposited submicrometer-wide strips of chromium atoms. Figure 2a schematically shows the focusing of atoms by a standing light wave, and Fig. 2b displays the deposited strips of chromium atoms, which are significantly narrower than the radiation wavelength.

2.2 Fabrication of atomic nanostructures on the basis of laser nanofields

Atom optics reliant on traveling and standing laser fields has several fundamental and technical restrictions arising from the spatially nonlocalized nature of the laser light fields. The nonlocalizability of the laser light field is responsible for the nonlocalizability of atom-optics elements. This gives rise to imperfections in atom-optics elements: aberrations of atom lenses, low diffraction efficiency of atomic waves, limitations on the contrast ratio for interference fringes in atomic interferometers, etc.

It is clear from general physical considerations that the use of spatially localized atom–field interaction potentials is preferable in the construction of atom-optics elements, the atom lens in particular. Only three types of laser fields with sufficient spatial localization are known today: (i) a surface light wave which emerges in the total internal reflection of light (one-dimensional localization of light); (ii) the light field which emerges in the diffraction of light by structures shorter than the light wavelength (two-dimensional localization of light); (iii) the light field localized in partially open waveguides — a 'photon dot' and a 'photon hole' (three-

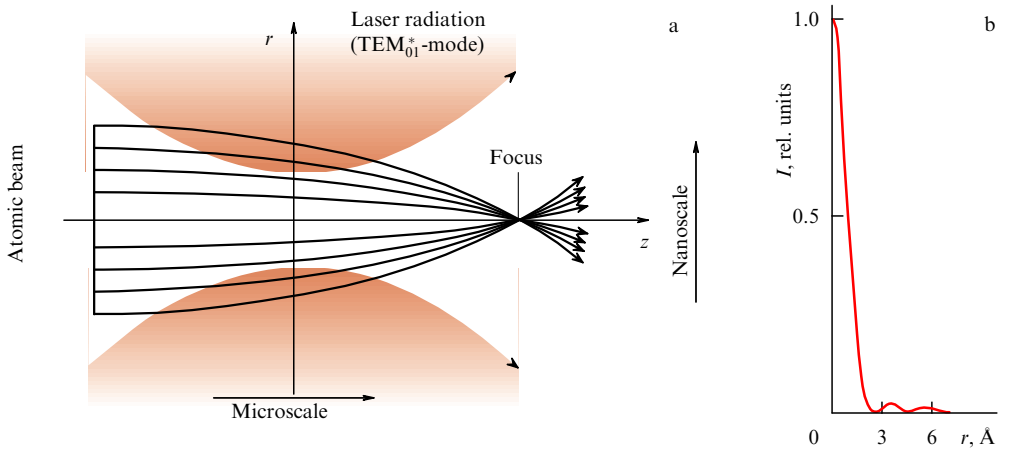

Figure 1. (a) Focusing of atoms on an angström-sized domain using the TEM_{01}^{*} mode. (b) Atomic density distribution with a width of about 1 Å in the focal plane of the atom lens.

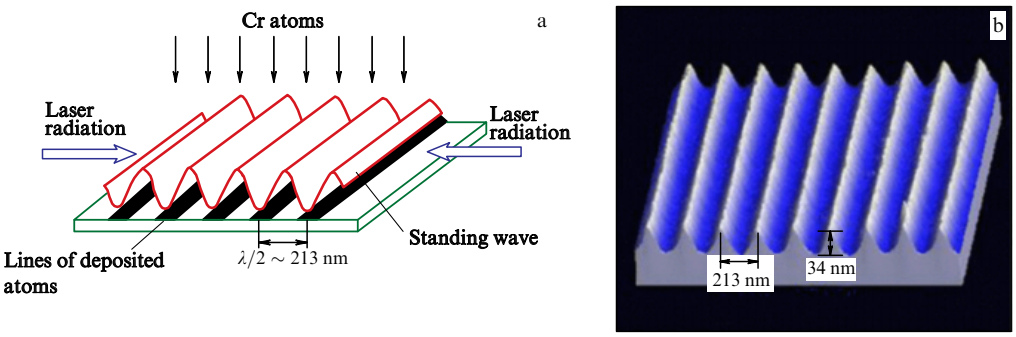

Figure 2. (a) Schematic sketch of the focusing of atoms by a standing light wave. (b) Deposited strips of chromium atoms with submicrometer widths.

dimensional localization of light). The last two laser nanofields have found application in atom lithography.

2.2.1 Atom lens on the basis of a Bethe hole. The best-known example of two-dimensional light localization is given by the Bethe aperture: a hole in a thin conducting screen with a diameter much smaller than the radiation wavelength [27–30]. The feasibility of applying such a nanolocalized field for the purposes of focusing atomic beams was studied in Refs [31–34]. It was shown [32–35] that a set of near-field microlenses may be employed to fabricate micro- and nanostructures on a surface.

A single near-field atom lens is schematically shown in Fig. 3a. Laser light is incident on a conducting screen with a hole smaller in diameter than the light wavelength. The field at the upper side of the screen consists of a traveling wave and the near-field component. The latter exhibits the follows remarkable features: (1) the magnitude of the near-field component in the immediate vicinity of the hole is on the order of magnitudes of the incident field; (2) the near-field component decays outside of the screen for a characteristic length on the order of the hole size, and (3) the near-field component possesses axial symmetry in a plane parallel to the screen and its magnitude varies approximately as the distance squared from the axis to the hole. The exact formal solution to the problem of plane wave diffraction by a round aperture in an infinitely thin metal plane was obtained in Refs [27–30]. Figure 3b demonstrates the near-field distribution of the light field.

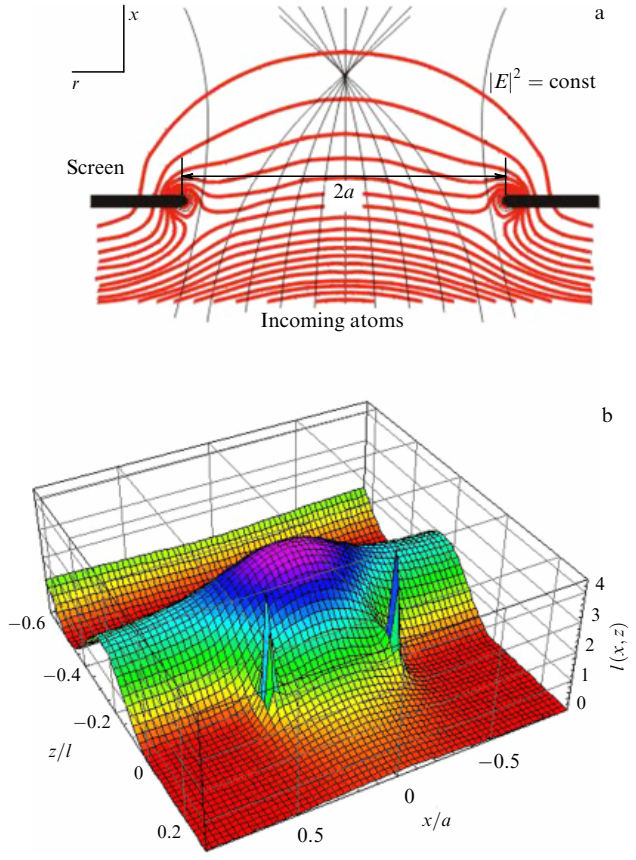

Figure 3. (a) Atom lens on the basis of light diffraction by the Bethe hole. (b) Near-field intensity distribution of the light field in the diffraction of light by the Bethe hole.

An analysis of near-field atom focusing [32–35] has revealed that efficient focusing may be accomplished for a relatively slow atomic beam. For a high atomic velocity, the short time of atom–field interaction confines the effect of the field on the atom, while for a low atomic velocity, the at-the-focus atomic beam dimension is limited by diffraction. The minimal focal spot size is defined by several factors which include: (1) spherical aberrations; (2) chromatic aberrations; (3) diffraction of atoms by the aperture; (4) the finite divergence of the incident atomic beam; (5) the interatomic interaction for a sufficiently high density, and (6) spontaneous emission. When these factors are taken into consideration, the focal spot size is equal to 0.1 of the optical wavelength.

2.2.2 Atom lens based on the 'photon dot' and 'photon hole'. A significant drawback of a field localized near an individual hole employed as an atom microlens is the fact that this field is inseparably linked with the field of the attached standing wave. In the motion of atoms in this domain, spontaneous decay processes may occur, which are ordinarily undesirable in atom lithography problems. We have investigated new types of spatially localized laser light fields with a characteristic dimension lying in the nanometer range, which are free from the above drawback [34, 36].

The scheme for obtaining this spatially localized light nanofield is depicted in Fig. 4a. Two plane conducting screens spaced at a distance of the order of or shorter than the light wavelength make up a planar two-dimensional waveguide for the laser radiation injected into it from one side. As is well known, for a waveguide consisting of two perfectly conducting parallel planes there exist solutions of the Maxwell equations which permit radiation propagation through a waveguide of arbitrarily small thickness d, including that significantly smaller than the radiation wavelength.

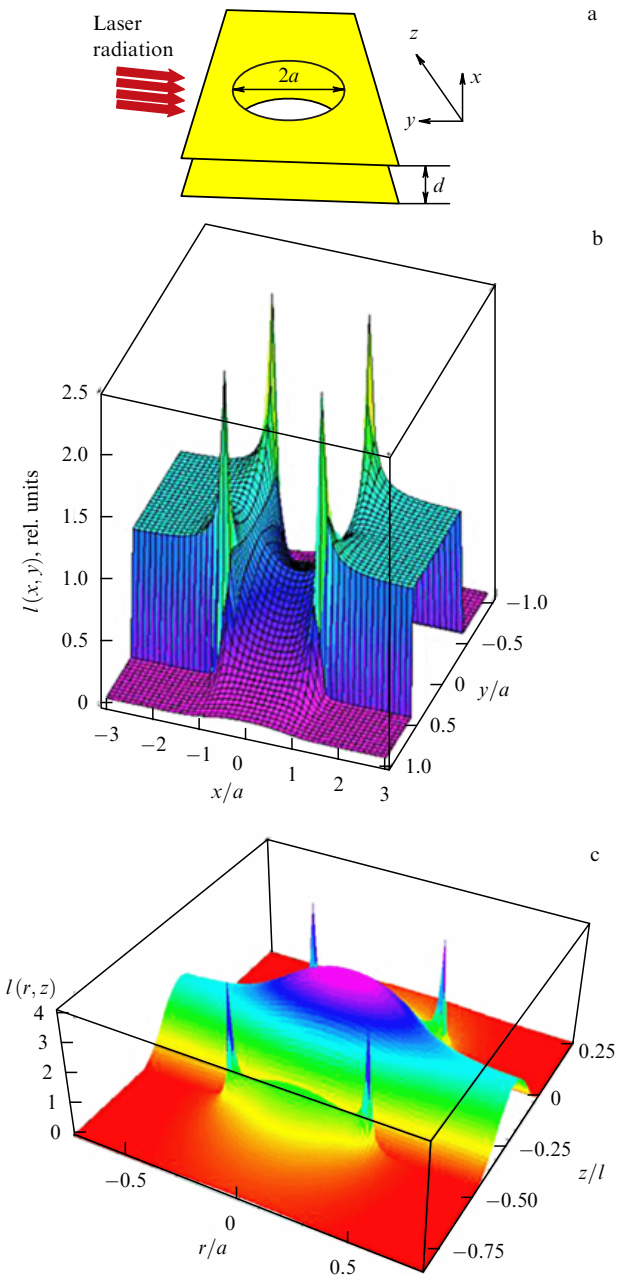

Figure 4. Three-dimensional nanolocalization of light. (a) Scheme for obtaining a spatially localized light nanofield: two conducting screens with a distance d between their planes, which is of the order of or smaller than the light wavelength, make up a planar two-dimensional waveguide for laser radiation injection into it from one side. (b) Energy density distribution for the electric field of the 'photon hole'. (c) Energy density distribution for the electric field of the 'photon dot'.

When the conducting screens have two small coaxial holes of radius a significantly smaller than the input radiation wavelength, $a \ll \lambda$, the radiation can hardly escape through these holes. However, the radiation traveling along the waveguide would be strongly modified in the vicinity of the holes. Near the holes there actually occurs field lowering in the domain with a characteristic spatial dimension of the order of the hole diameter, i.e., substantially smaller than the radiation wavelength. The volume of this domain is $V \ll \lambda^3$. Field modification near the holes depends on the polarization of the laser field inside the waveguide. Figure 4b demonstrates the energy density distribution for radiation with the electric field vector perpendicular to the plane of the waveguide. Field modification of this kind was termed a 'photon hole' [34]. One can see that in the vicinity of the holes there forms a photon hole whose characteristic dimensions are specified by the hole diameters and the waveguide thickness.

Figure 4c depicts the field intensity distribution near the hole of a planar waveguide and inside the waveguide, when the electric field vector of laser radiation is parallel to the waveguide plane, the waveguide thickness is equal to half the wavelength, and the hole radius $a = \lambda/2$. As is evident from the figure, the field decays quite rapidly outside of the waveguide in the direction perpendicular to the waveguide plane and peaks in the middle of the waveguide, i.e., a 'photon dot' forms. The characteristic volume of such a photon dot is also smaller than λ^3. The sharp field intensity peaks at the aperture edge are attributable to the assumption that the waveguide walls possess infinite conductivity. It is significant that the height of the maximum of the field in the middle of the holes is now twice the height of the maximum in the case of one hole. This circumstance, which is due to the constructive interference of the fields scattered by the holes, permits using lower fields than in the case of a single hole.

The photon dot and the photon hole may be employed to focus atomic beams by the gradient force which is proportional to the intensity of the electric field [34, 36]. For a positive detuning of laser radiation frequency relative to the atomic radiation frequency, the atom is forced into the lower-field domain; for a negative detuning, the atom is pulled into the higher-field domain.

2.3 Atom nanopen lithography

Nanopen lithography is a way of constructing arbitrary structures on a surface, which is similar to the deposition of ink lines on paper using a pointed pen. To draw such lines on a nanoscale calls for a nanopen. In the first nanopens (developed at Northwestern University, USA), atomic-force microscope probes were used as the pen. In this nanolithography technique, the reservoir of atom-ink is at the tip of the scanning probe which travels along the surface to leave behind it atom-sized lines. A serious disadvantage of the method is the long duration of the nanostructure fabrication procedure.

A nanometer hole in a screen on which an atomic beam is incident makes up an *atom pen* [37]. Atoms transmitted through the nanohole produce a nanospot on the surface behind the screen. By transferring the nanohole it is possible to produce nanostructures of arbitrary profile. The number of holes may be very large ($\sim 10^7$), which permits realizing parallel atom nanofabrication. Figure 5 shows one of the nanostructures made of Cr atoms with the aid of an atom nanopen [37]. The half-width of these nanostructures equals 170 nm.

2.4 Atom pinhole camera with a nanometer resolution

Despite the multiplicity of suggestions concerning the focusing of atomic beams by laser radiation, experimentally this remains a difficult problem. The main difficulty consists in the formation of an electromagnetic field – atom interaction potential which would be close in properties to a 'perfect' lens for atoms.

We experimentally realized [38] for the first time a different approach to the problems of focusing and constructing images in atom optics, which relies on the well-known idea of a pinhole camera employed both in light optics and in

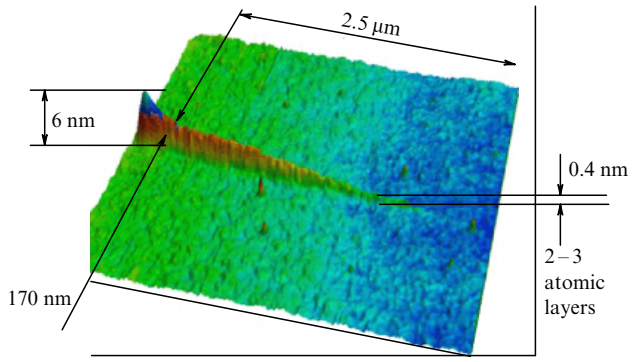

Figure 5. Nanostructure of Cr atoms made in the form of a varied-height strip with the help of an atom nanopen. The nanostructure half-width is 170 nm [37].

modern experimental physics when the focusing potential formation involves difficulties [39]. A pinhole camera in optics is a lens-free camera. The image-forming light passes through a hole which has to be small enough to produce a sharp image.

Figure 6 illustrates the schematic diagram of the experiment with an atom pinhole camera. An atomic beam is transmitted through a set of holes in a metallic mask to form, by analogy with optics, a 'luminous object' with a prescribed geometry. The atoms transmitted through the holes in the mask travel in a vacuum along rectilinear trajectories, like light beams, to arrive at a thin film with a large number of cone-shaped openings, which is located at a distance L from the mask. Each opening in the film is a pinhole camera for atoms, which forms an individual image of the object on the surface of a substrate positioned at a short distance l behind the film. In this geometry, a set of object images demagnified by about a factor of $m = L/l$ is produced on the substrate by the atoms deposited on its surface. In experiment, the object-forming mask was placed in the immediate vicinity of the source of atoms. For a thin film with openings, advantage was taken of a 5-μm thick track membrane with an asymmetric structure [40] and opening diameters $d = 20-1000$ nm.

In the experiment under discussion, every pinhole camera produces an image 'spot' of radius $a = (d/2)(1 + 1/m)$ in the plane of the substrate surface. The geometrical atom optics approximation is realized under the following limitation on

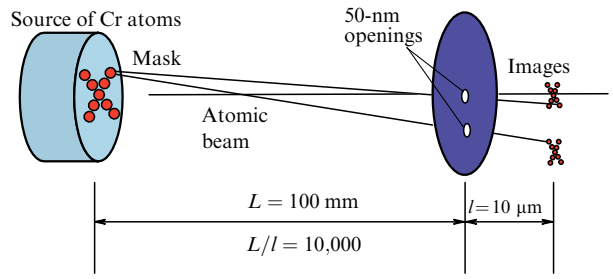

Figure 6. Schematics of a pinhole camera for atoms. A beam of Cr atoms transmitted through a set of holes in a metallic mask forms a 'luminous object' with a prescribed geometry. The atoms pass through the holes in the mask and travel along rectilinear trajectories to arrive at a thin film with openings. Each opening in the film is a pinhole camera for atoms and forms an inverted object image on a substrate.

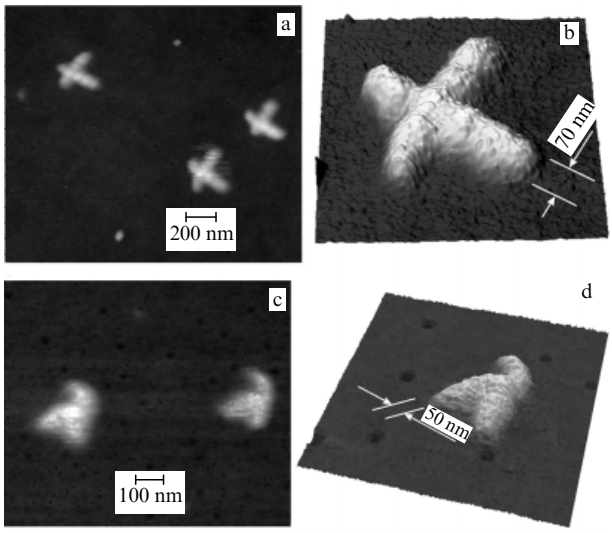

Figure 7. Nanostructures of Cr atoms on a glass surface, produced with an atom pinhole camera and a mask-object in the form of a cross: the areas of substrate portions are (a) 2 × 2 μm, and (b) 800 × 800 nm. Nanostructures of Cr atoms for a mask-object in the form of the letter λ: the areas of substrate portions are (c) 1 × 1 μm, and (d) 500 × 500 nm.

the de Broglie wavelength λ_{dB}: $1.22\,(\lambda_{dB}/d)\,l \ll d\,(1 + 1/m)$. In this case, the image, which is the inverted copy of the object demagnified by a factor m, has a resolution of the order of d, which permits producing nanometer-sized structures.

In the experiment, the average speed of Cr atoms in the beam was equal to about 900 m s^{-1}, which corresponds to the de Broglie wavelength $\lambda_{dB} = 0.08$ Å. The diffraction of atoms by the atom pinhole camera may be neglected for this wavelength.

Figures 7a and 7b display the Cr atomic nanostructures on a glass surface, which were obtained using an atom pinhole camera and a 'mask-object' in the form of a cross. Shown are portions of the substrate with areas of 2 × 2 μm (Fig. 7a) and 800 × 800 nm (Fig. 7b). The nanostructures were studied employing a scanning atomic-force microscope. Along with nearly complete images of the cross, the picture also presents structures that are images of only its part. This takes place due to a partial blocking of the atoms that form the image of the cross, which arises from the nonparallelism of the axes of different openings in the track membrane.

Figure 7b exhibits the detailed, most complete image of one of the crosses. The nanostructure base width is about 110 nm, which corresponds to the rectilinear passage of the beam's atoms through the openings in the pinhole cameras, and it is determined by the sum of their inlet diameter $d =$ 50 nm and the mask image diameter $d = 0.5$ mm$/8000 =$ 62 nm. The half-width of the nanostructure is equal to 70 nm.

Figures 7c and 7d give the results of an experiment involving the use of a mask in the form of the Greek letter lambda. The dimensions of this mask were smaller than the 'cross' type mask, with a consequential increase in the fraction of complete nonvignetted images. One can see from the figure that the half-width of the nanostructures produced is equal to 50 nm.

Figure 8 shows a nanostructure fabricated from Cr atoms in the form of the letter lambda, which is the symbol of the Institute of Spectroscopy of the Russian Academy of Sciences.

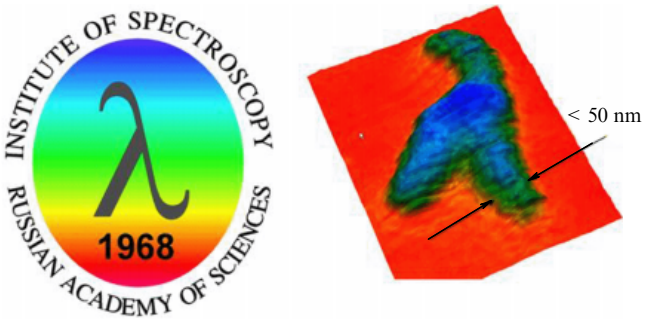

Figure 8. Cr atomic nanostructure in the form of the letter lambda, which is the symbol of the Institute of Spectroscopy of the Russian Academy of Sciences.

3. Summary

We have studied 'bottom up' approaches to nanotechnology, whereby the nanoobject being fabricated is assembled of individual atoms, molecules, biological cells, etc. The opportunity of realizing bottom up technology opened up with the development of probe microscopy techniques. However, the methods reliant on the use of scanning probes hold little attraction from the practical point of view, because they are characterized by a low productivity and a high cost. An alternative approach to bottom up nanotechnology is guided by atom optics. In this technique, the internal or external degrees of freedom of individual atoms are controlled by laser fields with nanometer precision, making it possible to produce surface structures at the nanometer scale.

References

1. Feynman R, http://www.zyvex.com/nanotech/feynman.html
2. Eigler D M, Schweizer E K *Nature* **344** 524 (1990)
3. Berggren K K et al. *Science* **269** 1255 (1995)
4. Rempe G, Schleich W (Eds) *Appl. Phys. B* **60** (2–3, Special Issue) 129 (1995)
5. Balykin V I, Letokhov V S *Atom Optics with Laser Light* (Laser Sciences and Technology, Vol. 18) (Chur: Harward Acad. Publ., 1995)
6. Arimondo E, Bachor H-A (Eds) *Quantum Semiclass. Opt.* **8** (3, Special Issue) 495 (1996)
7. Meystre P *Atom Optics* (Springer Series in Atomic, Optical, and Plasma Physics, Vol. 33) (New York: AIP Press/Springer, 2001)
8. Meschede D, Mlynek J (Eds.) *Appl. Phys. B* **70** (5, Special Issue) (2000)
9. McClelland J J "Nanofabrication via atom optics", in *Handbook of Nanostructured Materials and Technology* (Ed. H Nalwa) Vol. 1 (Cambridge: Academic Press, 1999)
10. Balykin V I, Klimov V V, Letokhov V S "Atom nano-optics", in *Handbook of Theoretical and Computational Nanotechnology* (Eds M Rieth, W Schommers) Vol. 7 (Amsterdam: Elsevier, 2006) p. 1
11. Balykin V I, Letokhov V S *Opt. Commun.* **64** 151 (1987)
12. Balykin V I, Letokhov V S *Zh. Eksp. Teor. Fiz.* **94** 140 (1988) [*Sov. Phys. JETP* **67** 78 (1988)]
13. Bjorkholm J E et al. *Phys. Rev. Lett.* **41** 1361 (1978)
14. Bjorkholm J E et al. *Opt. Lett.* **5** 111 (1980)
15. Gallatin G M, Gould P L *J. Opt. Soc. Am. B* **8** 502 (1991)
16. McClelland J J, Scheinfein M R *J. Opt. Soc. Am. B* **8** 1974 (1991)
17. Prentiss M et al. *Appl. Phys. Lett.* **60** 1027 (1992)
18. Cohen J L, Dubetsky B, Berman P R *Phys. Rev. A* **60** 4886 (1999)
19. Sleator T et al. *Appl. Phys. B* **54** 375 (1992)
20. Timp G et al. *Phys. Rev. Lett.* **69** 1636 (1992)
21. McClelland J J et al. *Science* **262** 877 (1993)
22. McGowan R W, Giltner D M, Lee S A *Opt. Lett.* **20** 2535 (1995)
23. Gupta R et al. *Phys. Rev. Lett.* **76** 4689 (1996)
24. Celotta R J et al. *J. Appl. Phys.* **79** 6079 (1996)
25. Drodofsky U et al. *Microelectron. Eng.* **30** 383 (1996)
26. Mützel M, Haubrich D, Meschede D *Appl. Phys. B* **70** 689 (2000)
27. Bethe H A *Phys. Rev.* **66** 163 (1944)
28. Meixner J, Andrejewski W *Ann. Phys.* (Leipzig) **59** 3318 (1950)
29. Nomura Y, Katsura S *J. Phys. Soc. Jpn.* **10** 285 (1955)
30. Levitan Y *J. Appl. Phys.* **60** 1577 (1986)
31. Klimov V V, Letokhov V S *Opt. Commun.* **106** 151 (1994)
32. Balykin V I, Klimov V V, Letokhov V S *J. Phys. II* (France) **4** 1981 (1994)
33. Balykin V I, Klimov V V, Letokhov V S *Pis'ma Zh. Eksp. Teor. Fiz.* **59** 219 (1994) [*JETP Lett.* **59** 235 (1994)]
34. Balykin V I, Klimov V V, Letokhov V S *Pis'ma Zh. Eksp. Teor. Fiz.* **78** 11 (2003) [*JETP Lett.* **78** 8 (2003)]
35. Balykin V, Klimov V, Letokhov V *Opt. Photon. News* **16** (3) 44 (2005)
36. Balykin V I, Minogin V G, Rudnev S N *Zh. Eksp. Teor. Fiz.* **130** 784 (2006) [*JETP* **103** 679 (2006)]
37. Balykin V I et al. *Zh. Eksp. Teor. Fiz.* (in press)
38. Balykin V I et al. *Pis'ma Zh. Eksp. Teor. Fiz.* **84** 544 (2006) [*JETP Lett.* **84** 466 (2006)]
39. Li Y T et al. *Phys. Rev. E* **69** 036405 (2004)
40. Apel P Yu et al. *Nucl. Instrum. Meth. B* **209** 329 (2003)

PACS numbers: 61.46.Fg, **85.85.+j,** 87.80.Mj

DOI: 10.1070/PU2007v050n07ABEH006323

Properties and nanotechnological applications of nanotubes

Yu E Lozovik, A M Popov

1. Introduction

The last decade has seen considerable progress in nanomechanics. In particular, the feasibility of manipulating nanometer-sized objects has been demonstrated [1] and basic designs for nanoelectromechanical systems (NEMSs) which can realize controllable motion of nanoobjects have been considered [2]. The search for nanoobjects that may be employed as the movable elements of NEMSs is currently a topical problem. The possibility of arbitrary [3, 4] relative motion of walls in multi-walled carbon nanotubes [7] that is controllable with an atomic-force microscope [5, 6] and the extraordinary elastic properties of carbon nanotube walls [8–12] make them challenging candidates for NEMS elements. Several nanomechanisms have been suggested, which are based on the relative sliding or rotation of nanotube walls: a nanobearing [13], a nanogear [14], a nanoswitch [15], a nanorelay [16, 17], a gigahertz oscillator [18, 19], and a Brownian nanomotor [20, 21]. The unique electronic properties of carbon nanotubes [22] find use in experimentally realized electronic nanodevices like nanotransistors [23], nanodiodes [24], current nanomodulators [25], etc. Furthermore, nanomotors reliant on the relative rotation of carbon nanotube walls have been made recently [26, 27]. In the nanoresistor, nanorelay, and nanomotor mentioned above, the nanotube walls are simultaneously movable NEMS elements and elements of an electric circuit. This family of carbon nanotube applications in NEMSs embraced a new unique and promising application: specifically, it was shown that a double-walled carbon nanotube (DWNT) could be a pair with an effective 'screw thread' [28–32]. In this connection, basic designs were proposed for NEMSs based on carbon nanotubes whose structure comprises a 'nanobolt–nanonut' pair: a 'nanodrill' for nanolocal surface

modification [28 – 30, 32] and a nanoactuator for the transformation of a force directed along the nanotube axis to the relative rotation of its walls [17, 32, 33]. According to calculations, the nanotube conductivity significantly changes under a minor relative displacement (by a fraction of an angström) of its walls along the nanotube axis [34 – 36] or a relative rotation of the walls [37]. We came up with the idea of employing this nanotube property in such NEMSs as a variable nanoresistor [28 – 30], tension nanosensor [38], and electromechanical nanothermometer [17, 39].

Carbon nanotubes are promising candidates for utilizing in NEMSs based not only on the relative motion of nanotube walls, but also on nanotube bending. Of these NEMSs mention should primarily be made of nanooscillators in which measurements of the frequency of transverse nanotube modes are employed for measuring the properties of a system. For instance, by measuring the vibration frequency of a nanotube fixed at one end it was possible to determine the mass of a nanoparticle and even of a single molecule located at the other end of the nanotube [11]; in addition, a nanodevice was realized which allowed, by measuring the vibration frequency of a nanotube fixed at both ends, measuring the force acting on the nanotube with an accuracy of 5×10^{-18} N [40]. Furthermore, nanotweezers were made, which capture nanoparticles and manipulate them by bending the ends of two nanotubes via electrostatic forces [41, 42], as was a memory cell of two intersecting nanotubes [43].

This report is concerned with NEMSs based on carbon nanotubes with movable walls. The properties and structure of nanotubes are described in Section 2. The interaction and relative motion of nanotube walls are considered in Section 3. Ways of controlling the motion of nanotube walls and NEMS operating modes are discussed in Section 4. Section 5 is dedicated to the basic designs and operating principles of carbon nanotube-based NEMSs. Finally, considered in Section 6 is the development of nanotechnology methods which may be employed to fabricate carbon nanotube-based NEMSs.

2. Structure and properties of nanotubes

2.1 Structure of single-walled nanotubes

A single-walled carbon nanotube (SWNT) may be represented as a single graphite plane rolled up (graphene). The SWNT structure is defined by the pair of integers (n, m) — chirality indices, which are the coordinates of the graphene lattice vector $\mathbf{c} = n\mathbf{a}_1 + m\mathbf{a}_2$ (where $\mathbf{a}_1$ and $\mathbf{a}_2$ are the unit vectors of the graphene plane). The segment corresponding to the vector $\mathbf{c}$ becomes, on rolling up a graphene plane fragment into an SWNT, its circumference (Fig. 1) [22, 44]. The wall radius R is defined by the expression

$$R = \frac{|\mathbf{c}|}{2\pi} = \frac{a_0\sqrt{n^2 + mn + m^2}}{2\pi}, \qquad (1)$$

where $a_0 = 0.246$ nm is the length of the unit vector of the graphene plane. The SWNT radius typically is on the order of several nanometers; the shortest SWNT radius obtained is about 0.4 nm. The SWNT unit cell length is expressed as

$$b = \frac{\sqrt{3}a_0\sqrt{n^2 + mn + m^2}}{\mathrm{GCD}\,(2m + n, n + 2m)}, \qquad (2)$$

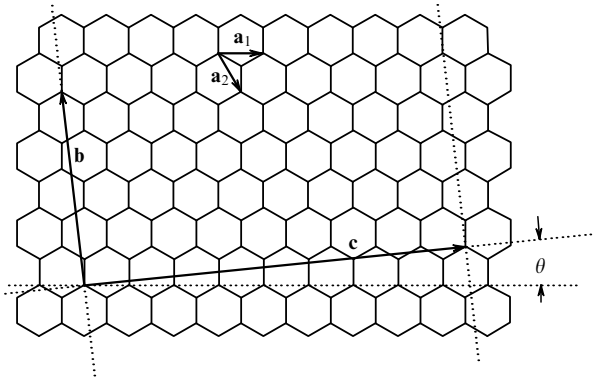

Figure 1. Graphite plane (graphene) rolled into a nanotube wall; $\mathbf{a}_1$ and $\mathbf{a}_2$ are the unit vectors of the graphite plane. The wall is unambiguously defined by the vector $\mathbf{c}$: the length of wall circumference is equal to $|c|$. The modulus of the vector $\mathbf{b}$ defines the unit cell length, and θ is the wall chirality angle.

where $\mathrm{GCD}\,(u, w)$ is the greatest common divisor of the integers u and w. The chirality angle θ is defined as the angle between the vectors $\mathbf{a}_1$ and $\mathbf{c}$:

$$\theta = -\arccos\frac{2n + m}{\sqrt{n^2 + m^2 + mn}}. \qquad (3)$$

Since the graphite plane is sixth-order symmetrical, only the SWNTs defined by vectors $\mathbf{c}$ that lie within an angle of 60°, i.e., with $m > 0$ and $n > 0$, are nonequivalent. Single-walled carbon nanotubes with the chirality indices (n, n) — an 'armchair' — and $(n, 0)$ — a 'zigzag' — are nonchiral, whereas all the rest of the SWNTs are chiral. In this case, SWNTs with chirality indices (n, m) and (m, n) are mirror-symmetric, i.e., are structurally left-helical for $n > m$, and right-helical for $m > n$.

2.2 Electronic properties of nanotubes

As is well known, a graphene sheet possesses an electronic structure with a linear dispersion law in the conduction and valence bands (i.e., the effective masses of electron and hole excitations are equal to zero) and a zero energy gap. Rolling up the graphene sheet results in band confinement (addition), with the effect that there appear 'transverse quantization' subbands, depending on chirality indices. As a result, the SWNTs with chirality indices (m, n) are metallic, when the condition $m + n = 3q$ is satisfied, where q is an integer [22], and are semiconducting in the remaining cases.

2.3 Elastic properties of nanotubes

Both SWNTs [45, 46] and multi-walled carbon nanotubes (MWNTs) up to 30 μm in length [47] and containing several dozen walls [7] have been obtained. Multi-walled carbon nanotubes have the structure of nested coaxial walls, similar to the graphite structure, with an interwall distance of about 0.34 nm [7], which is close to the spacing between graphite layers. That is why graphite and nanotubes possess similar elastic properties. In particular, the experimental elastic modulus for graphite compression along the layers amounts to 1.24 TPa [48], which is approximately five times greater than the elastic modulus for steel.

The elastic properties of nanotubes, including their plastic deformation under a heavy load, were considered at length in the review [49], and therefore in this report we restrict

ourselves to a brief enumeration of the main results. Numerous experiments have yielded a value of about 1 TPa for the Young modulus. Specifically, measurements of the force required for bending an MWNT, an SWNT, and SWNT bundles yielded Young moduli of 1.28 ± 0.59 TPa [9], 1.2 TPa [50], and 1.18 ± 0.4 TPa [51], respectively. Measurements of the force required for the extension of nanotubes yield values of the Young modulus of 0.27–0.95 TPa for MWNTs [3] and 0.32–1.47 TPa for SWNT bundles [52]. Young moduli of 1.8 ± 1.4 TPa for MWNTs [8] and 0.32–1.47 TPa for SWNT bundles [10] were derived from an analysis of the thermal vibrations of nanotubes fixed at one end. Investigation into the electromechanical vibrations of MWNTs fixed at one end shows that their flexural modulus increases from 0.1 to 1 TPa as the nanotube diameter decreases [11].

The experimental values of the Young modulus agree well with the theoretical estimates. Values of the Young modulus for different SWNTs, obtained by way of calculations based on the density functional theory, range between 0.94 and 1.09 TPa [53–57]. Values of the Young modulus close to 1 TPa were also obtained via semiempirical methods [58–61].

3. Interaction and relative motion of nanotube walls

The force causing the relative motion of nanotube walls is defined by the expression

$$F = F_{\mathrm{f}} + F_{\mathrm{W}} = \pi D \tau L_{\mathrm{ov}} + \gamma \pi D + F_{\mathrm{e}}\,, \tag{4}$$

where F_{f} is the force of static and dynamic friction, F_{W} is the van der Waals force which retracts the inner wall into the outer one in the telescopic extension of the former, D is the diameter of the movable wall, L_{ov} is the wall overlap length, τ is the wall shear modulus which includes the dynamic and static shear moduli, γ is the interwall interaction energy per unit area of the wall overlap surface, and F_{e} is the static friction force related to the interaction between the edge of one wall and the surface of the other one. By way of investigations into the interwall interaction force with the aid of atomic-force microscopy [6] it was determined that the interwall interaction energy γ ranges from 22 to 33 meV per atom for different nanotubes. This value is consistent with the estimate obtained from the geometrical characteristics of flattened nanotubes: $\gamma = 35 \pm 10$ meV per atom [62], and with the data calculated by the method of density functional for different nanotubes: $\gamma = 18-21$ meV per atom [63], and $\gamma = 23-24$ meV per atom [12]. This interwall interaction energy corresponds to values of the van der Waals force from 0.5 to 20 nN, depending on the diameter of the movable wall. Forces in this range are typical for atomic-force microscopy (see the review [64]), and the relative motion of walls may therefore be controlled using a nanomanipulator.

The above experiments [6] revealed no energy dissipation in the relative motion of walls and showed that the force required for the telescopic extension of the inner wall is independent of the wall overlap length. These results yield upper estimates for the dynamic and static shear moduli of 0.05 and 0.04 MPa, respectively. The experimental value of the shear modulus for graphite layers is about 1 MPa [65]. The substantially lower value of the shear modulus for nanotube walls in comparison with the shear modulus for graphite layers is explained as follows: graphite layers are always commensurate, while nanotube walls may be both commensurate and incommensurate.

The walls of a nanotube are commensurate when the ratio b_1/b_2 between the unit cell lengths is a rational fraction. The characteristics of the interaction and the relative motion of commensurate and incommensurate nanotube walls are theoretically analyzed below by the example of DWNTs. In the case of commensurate walls, a DWNT is a one-dimensional crystal with the unit cell length equal to the least common multiple of the unit cell lengths of the walls.

Recently, a classification scheme was proposed for DWNTs with commensurate walls [66, 67]. According to this scheme, these double-walled nanotubes make up families. All nanotubes of each family have equal unit cell lengths, interwall distances, and chirality angles for the inner and outer walls. This classification is simultaneously a classification for the possible pairs of commensurate neighboring MWNT walls and may be employed for the selection of such pairs which show promise for NEMS (for instance, for the selection of neighboring walls in a nanoactuator [33]). A table comprising the complete list of all possible DWNT families with commensurate walls is given in Ref. [66].

To investigate the characteristics of relative motion of nanotube walls, it is required to calculate how the interaction energy U for two neighboring walls depends on the coordinates describing the relative position of the walls: the angle ϕ of the relative wall rotation about the nanotube axis, and the length z of the relative wall displacement along this axis. The potential relief $U(z,\phi)$ of interwall interaction energy is conveniently visualized by developing the cylindrical surface. The symmetry transformations of the function $U(z,\phi)$ comprise all symmetry transformations of both the walls. There are four combinations of neighboring wall pairs with basically different potential reliefs of their interaction energy: (1) commensurate nonchiral walls; (2) commensurate walls, at least one of which is chiral; (3) incommensurate walls, and (4) commensurate walls, at least one of which is chiral and the other possesses periodically located defects in atomic wall structure.

For a DWNT with commensurate nonchiral walls $\big((n,n)@(m,m)$ and $(n,0)@(m,0)\big)$, an expression was derived for the expansion of the interwall interaction energy into a Fourier series [68]:

$$\begin{aligned} U(z,\phi) &= \sum_{M,\,K\,(\mathrm{odd})=1}^{\infty} \alpha_K^M \cos\left(\frac{2\pi}{b} Kz\right) \cos\left(\frac{nm}{N} M\phi\right) \sin^2\left(\frac{\pi nm}{2N^2}\right) \\ &+ \sum_{M,\,K\,(\mathrm{even})=0}^{\infty} \beta_K^M \cos\left(\frac{2\pi}{b} Kz\right) \cos\left(\frac{nm}{N} M\phi\right), \end{aligned} \tag{5}$$

where N is the greatest common divisor of n and m, and b is the length of an individual DWNT cell. Even terms are always present in expansion (5), while odd terms are present only when both the ratios, n/N and m/N, are odd. According to the topological theorem [69], the critical points of the interwall interaction energy $U(z,\phi)$ correspond to the relative positions of the walls for which the second-order symmetry axes U_2 of the two walls coincide. The axes U_2, perpendicular to the principal wall axis, pass through this axis and the middle of the bond or the center of the hexagon in the wall structure. The elementary cell of the function $U(z,\phi)$ for a DWNT with commensurate nonchiral walls contains four critical points: a minimum, a maximum, and two saddles. The

relative wall positions corresponding to the critical points are described in Ref. [12].

The amplitudes of the harmonics in expansion (5) decrease exponentially with harmonic numbers M and K [69 – 71]. That is why the interwall interaction energy $U(z, \phi)$ for a DWNT with commensurate nonchiral walls may be approximated with only the first two terms of expansion (5):

$$U(z, \phi) = U_0 - \frac{\Delta U_\phi}{2} \cos\left(\frac{2nm}{N}\,\phi\right) - \frac{\Delta U_z}{2} \cos\left(\frac{4\pi}{b}\,z\right), \tag{6}$$

where U_0 is the average interwall interaction energy, and ΔU_ϕ and ΔU_z are the potential barriers for the relative rotation of the walls and for their sliding along the DWNT axis, respectively. In this case, U_0, ΔU_ϕ, and ΔU_z are defined by interpolation from the values of $U(z, \phi)$ at four critical points. Semiempirical calculations show, by the example of several dozen DWNTs with commensurate nonchiral walls, that the energy $U(z, \phi)$ can be approximated by expression (6) correct to about 1% [67]. This result is confirmed by the data of calculations done by the method of density functional for a DWNT (5,5)@(10,10) with an accuracy of about 5% [63].

The majority of DWNTs with commensurate nonchiral walls have incompatible wall rotation symmetries. For this reason, the angular period $\delta_\phi = 2nm/N$ of the energy $U(z, \phi)$ is short, and the potential barrier ΔU_ϕ for relative wall rotation is low (lower than 0.005 meV per atom according to calculations by the method of density functional [63], and lower than 10^{-11} meV per atom according to calculations employing semiempirical potentials [67]). In this case, the interwall interaction energy is approximately defined by the equation

$$U(z, \phi) \approx U_0 - \frac{\Delta U_z}{2} \cos\left(\frac{4\pi}{b}\,z\right). \tag{7}$$

The sole exceptions are provided by DWNT (5,5)@(10,10) [12, 31, 63, 71 – 73] and DWNT (9,0)@(18,0) [12, 67, 71], which exhibit significant barriers for relative wall rotation. The potential reliefs of the interwall interaction energy $U(z, \phi)$ for DWNTs (5,5)@(10,10) and (6,6)@(11,11), which possess compatible and incompatible wall rotation symmetries, are depicted in Figs 2a and 2b, respectively. We note that expression (5) is valid for all physical quantities which depend on the relative position of nonchiral commensurate DWNT walls, in particular, for the conductivity.

The potential relief is quite flat for any DWNT with commensurate walls, at least one of which is chiral. This is so because only very high harmonics of the Fourier transform of the interaction energy U_a between an atom of one wall and the entire other wall make contributions to the potential barriers due to the incompatibility of the helical symmetries of the walls [70]. For instance, the barrier for the relative wall rotation of a DWNT (8,2)@(16,4), which was calculated on the basis of the Lenard – Jones potential, is about 5×10^{-12} meV per atom, and this is the only example revealed to date in which the potential barrier for the relative motion of chiral commensurate walls exceeds (!) the limit of calculation accuracy [67]. The heights of other barriers for several dozen DWNTs with chiral commensurate walls considered are lower than the calculation accuracy [67]. A calculation based on the Crespi – Kolmogorov potential [74] also shows that the potential relief for all the defect-free

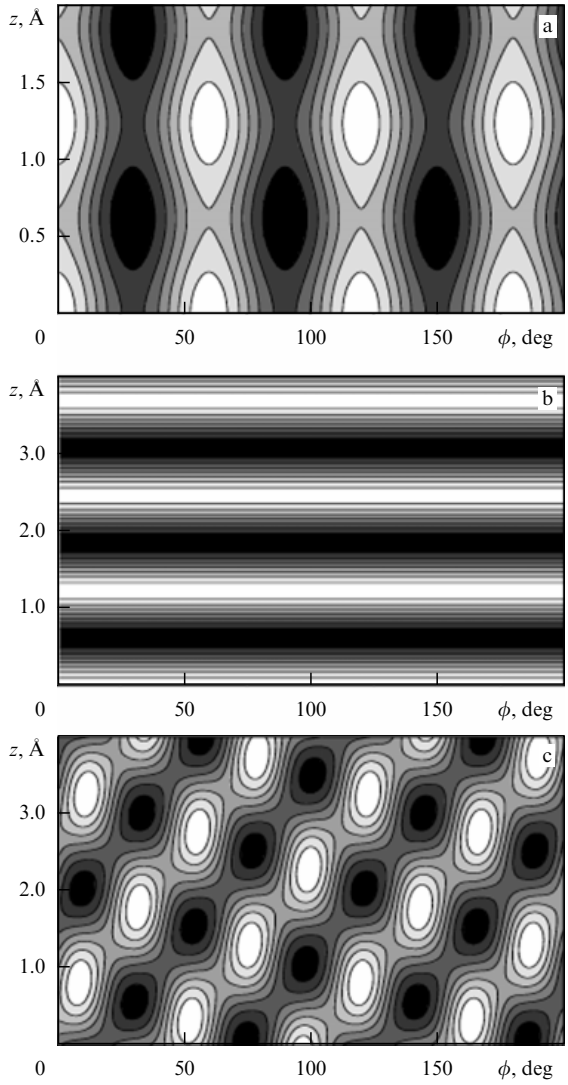

Figure 2. Potential reliefs of the interaction energy $U(z, \phi)$ for the walls of a double-walled nanotube as functions of the relative wall displacement z along the nanotube axis and of the angle ϕ of relative wall rotation about the axis for (a) DWNT (5,5)@(10,10), (b) DWNT (6,6)@(11,11), and (c) a DWNT with a vacancy in every unit cell of the inner wall. The energy is measured from its minimum. The equipotential lines in Figs 2a, 2b, and 2c are drawn at 4.0×10^{-3}, 1.0×10^{-3}, and 4.0×10^{-3} meV per atom intervals, respectively.

DWNTs under consideration that have commensurate walls, at least one of which is chiral, is extremely flat [71]. This result was borne out by calculations reliant on the method of density functional for a DWNT (8,2)@(16,4) [63].

In the general case, a nanotube wall possesses helical symmetry (see, for instance, Ref. [75]), and therefore the interwall interaction energy $U(z, \phi)$ also possesses helical symmetry. Consequently, the potential relief may have valleys directed along a helix, similar to the thread on the side surface of a bolt. In what follows such potential reliefs are termed reliefs of the thread type. Double-walled carbon nanotubes with thread type potential reliefs may be employed in NEMSs as a nanobolt – nanonut pair. Among the quantitative characteristics of this thread are the potential barriers E_1 and E_2 for relative DWNT wall motion along the thread line and for twisting-off the thread (motion across the thread), respectively, as well as the threshold forces for setting

the walls in relative motion along the thread line and for twisting-off the thread. The thread may be qualitatively characterized not only by potential barriers, but also by their ratio $\beta = E_2/E_1$ which is termed the relative depth of thread [28, 29]. It was nevertheless discovered that in those cases where DWNTs with defect-free walls may have a thread type relief the characteristics of this thread do not permit employing these DWNTs as a nanobolt – nanonut pair in NEMSs. Initially, the thread type relief was found in several DWNTs with incommensurate walls, in this case for simplicity one of the walls being assumed to be ultimately short — equal in length to that of the wall unit cell (normally equal to several nanometers or dozen nanometers) [31]. However, a detailed study revealed that the depth of thread of the potential relief for a DWNT with incommensurate walls is small and therefore the force required for twisting-off the thread is weak for any wall lengths [28, 29]. Moreover, the depth of thread varies significantly with the length of the short movable wall, and the thread type relief may even vanish for some values of the length of this wall [28, 29]. Therefore, a DWNT with incommensurate walls may be employed as a nanobolt – nanonut pair with the desired depth of thread only when the short wall length corresponds to within several angströms to the prescribed one. The feasibility of fabricating such a DWNT is highly conjectural. Since nonchiral walls possess planes of mirror symmetry passing through the principal wall axis [68], the potential relief of these DWNTs also possesses suchlike mirror symmetry planes and, hence, may not be a thread type relief [32, 76]. As mentioned above, for DWNTs with commensurate walls, at least one of which is chiral, the potential relief is rather flattened due to the incompatibility of wall symmetries, and therefore all the potential barriers for the relative motion of walls are extremely low. Furthermore, a detailed consideration of the potential relief symmetries of these DWNTs reveals that most of them may not possess a thread type potential relief at all [32, 76].

It turns out that the presence of defects in an atomic wall structure radically changes the situation. Specifically, due to the occurrence of defects, even the first harmonic of the Fourier transform of the interaction U_a between an atom of one wall and the entire other wall makes a nonzero contribution to the potential barriers. According to several calculations, this results in an increase in the corresponding barriers by 8 – 10 (!) orders of magnitude [32, 67, 76, 77]. This property of a DWNT with atomic structure defects may be employed to obtain a DWNT with a thread type relief whose characteristics allow using such a DWNT as a nanobolt – nanonut pair in NEMSs. It has been suggested that similar artificial defects should be produced at identical sites in a large number of unit cells of DWNTs with commensurate walls [32, 67, 76, 77]. In this case, any barrier ΔU for relative motion of walls is defined by the expression $\Delta U = \Delta U_u N_u$, where ΔU_u is the barrier for one nanotube cell, and N_u is the number of cells with defects. Therefore, the 'atomic design' of the DWNT structure permits obtaining the nanobolt – nanonut pair with desired (high enough) barrier values which prevent the thread from being twisted-off in the case of sufficiently long nanotubes. A theoretical investigation was made to elucidate how the thread characteristics are affected by a 'substituted atom' defect structure and by the potential parameters for the interaction between the atom corresponding to the defect and the atoms of the defect-free wall [32, 76]. It was found that the relative depth of thread $\beta = E_2/E_1$ (which characterizes its quality) depends only slightly on the above quantities and consequently is determined by the structure of the defect-free wall. An example of a thread type potential barrier for a DWNT with commensurate nonchiral walls and periodically sited defects is given in Fig. 2b.

4. Nanoelectromechanical systems: operating modes and ways of control

4.1 Modes of operation of nanoelectromechanical systems

To investigate the feasibility of utilizing the nanobolt – nanonut pair in NEMSs, an analysis was made of the relative motion of coaxial DWNT walls along the helical line of thread [28 – 30]. (The results of this analysis also apply to the special cases of helical motion — the relative rotation of the walls and their relative sliding along the DWNT axis.) The researchers underwent the analysis of the case where one wall was fixed and the other movable, while the forces acting on the movable wall did not lead to its deformation and displacement of its axis with respect to the axis of the fixed wall. For instance, this is possible when each atom of the movable wall experiences a force $\mathbf{F}_a$ consisting of two components which are the same for every atom: the force F_z aligned with the DWNT axis, and the force F_l aligned with the tangent to the wall circumference, passing through the atom. In the case under consideration, it is easily shown that the motion of the movable wall of mass M relative to the fixed wall is equivalent to the two-dimensional motion of a particle of mass M in the potential field of the interwall interaction energy $U(R\phi, z)$, where R is the movable wall radius, under the action of force $\mathbf{F} = (N_a F_z, N_a F_l)$. In this case, the wall motion along the helical line of the thread is equivalent to the particle motion along a straight line.

As the analysis suggests, when (i) the potential barrier for twisting-off the thread is significantly higher than the barrier for relative motion of walls along the line of thread, $E_2 \gg E_1$, (ii) the energy of thermal wall motion is significantly lower than the barrier heights for their relative motion, $kT \ll E_1, E_2$, and (iii) the force acting on the movable wall is weak, $F_x \delta/2 \ll kT$ (where F_x is the projection of force $\mathbf{F}$ on the line of the thread, and δ is the distance between the minima of potential relief along the line of the thread), the relative motion of walls along the line of the thread constitutes a drift and is described by the Fokker – Planck equation

$$\frac{\partial n}{\partial t} = D\,\frac{\partial^2 n}{\partial x^2} + \frac{\partial n}{\partial x}\,BF_x\,, \tag{8}$$

where x is the coordinate specifying the relative wall arrangement along the line of the thread, $n(x,t)$ is the probability distribution function for the relative wall arrangement, D is the diffusion coefficient:

$$D = \frac{1}{2}\,\Omega\delta^2 \exp\left(-\frac{U_1}{kT}\right), \tag{9}$$

B is the mobility:

$$B = \frac{\Omega\delta^2}{2kT} \exp\left(-\frac{U_1}{kT}\right), \tag{10}$$

and Ω is the pre-exponential factor in the Arrhenius formula for the frequency of wall jumps between the equivalent potential relief minima located in the line of the thread (by the order of magnitude, Ω is equal to the average frequency of

the relative vibrations of the walls along the line of the thread). We note that the Einstein relation $D = kTB$ is fulfilled.

The operating mode of NEMSs reliant on the relative motion of nanotube walls, when this motion is described by the Fokker – Planck equation, will be termed the stochastic mode [28 – 30]. A steady directional wall motion in the Fokker – Planck operating mode is possible when the average distance $x_{dr} = BF_x t$, which the wall travels along the line of the thread in a time t by virtue of the drift under the action of force **F**, exceeds the distance $x_{di} = \sqrt{2Dt}$ by which it shifts along this line due to diffusion:

$$BF_x t \gg \sqrt{2Dt}\,. \tag{11}$$

We substitute the Einstein relation $D = kTB$ into condition (11) to arrive at the conclusion that it is worthwhile employing the stochastic mode in NEMSs for an operating time

$$t > \frac{2k^2T^2}{F_x^2 D} \tag{12}$$

and wall drift displacements x_{dr} along the line of the thread:

$$x_{dr} \gg \frac{2kT}{F_x}\,. \tag{13}$$

On substituting into condition (13) the strongest force $F_x \approx 2kt/\delta$ for which the relative motion of walls is adequately described by the Fokker – Planck equation, we conclude that it is expedient to use the stochastic mode in NEMSs for $x_{dr} \gg \delta$, i.e., for several dozen relative wall jumps between the minima of the potential relief along the line of the thread. Such a wall displacement corresponds to about one turn about the nanotube axis and to a displacement along its axis by several nanometers. The stochastic mode may be employed in some of the NEMSs considered in Section 5, like nanomotors and nanoactuators.

For forces satisfying the condition $F_x\delta/2 \gg kT$, the stochastic component in relative motion of walls may be neglected. In this case, the motion of the walls is accelerated and is rather accurately described by the equation of motion. The NEMS operating mode which is based on the relative motion of nanotube walls and corresponds to such forces will be referred to as dynamic. This mode allows controllable relative displacement of the walls by any distance along the line of the thread. This operating mode may be employed, for instance, in variable nanoresistors.

The force **F** which sets the movable wall in motion relative to the fixed one may be resolved into two components: the force directed along the nanotube axis (a force of the 1st type), and the force aligned with the tangent to the circumference of the movable wall (a force of the 2nd type). When the potential relief corrugation has no effect on the relative motion of walls, the type of relative motion of walls corresponds to the type of forces applied. Specifically, type-1 forces give rise to the relative wall sliding along the nanotube axis, while type-2 forces lead to the relative rotation of the walls. However, when the potential relief corrugation exerts a significant effect on the relative motion of walls, this correspondence is generally absent. In particular, for a potential relief of the thread type the relative motion of walls along the helical line of the thread may be caused by the action of forces of both types (or their superposition) applied to the movable wall. The relative motion of walls along the helical line of the thread is simultaneously both the relative rotation and the relative sliding along the nanotube axis. Consequently, the type-1 force gives rise not only to the relative sliding of the walls along the nanotube axis, but also to their relative rotation, and the type-2 force effects not only the relative rotation of the walls, but also their relative axial sliding. In the former case, it is possible to create NEMSs operating like a whirligig. This way of setting the walls in relative rotation may be employed in the nanoactuators described in Section 5.6, which consist of a nanobolt – nanonut pair and nanotube-based nanobearings. In the latter case, it is possible to fabricate NEMSs operating like a faucet in which the rotation of a knob is transformed to the translational motion of the bar.

4.2 Ways of controlling the nanoelectromechanical systems

Control of NEMSs based on the relative motion of nanotube walls may be effected with the help of (i) a nanomanipulator, (ii) the pressure of a gas being heated and confined between the movable and fixed walls, (iii) a magnetic field, and (iv) an electric field.

The feasibility of controlling the relative motion of nanotube walls by way of a nanomanipulator attached to an atomic-force microscope has been demonstrated experimentally [5, 6]. The drawback of this method of controlling NEMS motion is the large dimensions of the nanomanipulator and the nanomanipulator motion control system in comparison with the dimensions of the NEMS itself.

The feasibility of relative motion of nanotube walls under the pressure of the gas being heated and confined between the movable and fixed walls was shown by simulations using the molecular dynamics method [78]. In Ref. [78] it was suggested that the gas inside a NEMS should be rapidly heated by a pulsed laser. However, this means of control cannot be used for continuous NEMS operation, because the NEMS has to be cooled after each single actuation of the movable wall.

When the movable wall is metallic or metal-filled and the remaining walls are semiconducting, it was suggested that the movable wall be driven by a nonuniform magnetic field [79]. When such a wall moves at a velocity V in a nonuniform magnetic field B, the variation of the magnetic flux Φ induces in the wall a current

$$i = -G\,\frac{\mathrm{d}\Phi}{\mathrm{d}t} = -GS\,\frac{\mathrm{d}B}{\mathrm{d}t} = -GSV\,\frac{\mathrm{d}B}{\mathrm{d}z}\,, \tag{14}$$

where G is the conductivity, and S is the wall cross-section area. The wall energy U_m in the magnetic field is defined by the expression

$$U_m = -\mu B = -SiB = -GS^2VB\,\frac{\mathrm{d}B}{\mathrm{d}z}\,, \tag{15}$$

where $\mu = Si$ is the magnetic dipole moment of the wall. The force F_m exerted by the magnetic field on the moving wall is expressed in the form

$$F_m = \frac{\mathrm{d}U_m}{\mathrm{d}z} = GS^2V\left[\left(\frac{\mathrm{d}B}{\mathrm{d}z}\right)^2 + B\,\frac{\mathrm{d}^2B}{\mathrm{d}z^2}\right]. \tag{16}$$

However, the experiments, simulations, and numerical estimates proving the feasibility of this way of controlling nanotube wall motion are utterly lacking to date.

The motion of the inner wall filled with a magnetic material may be controlled with the aid of a magnetic field. Several methods have been elaborated for the fabrication of

MWNTs containing magnetic materials inside of them [80–82]. However, the walls of nanotubes with magnetic materials, fabricated by these methods, contain too many defects, which makes unlikely the relative motion of such walls.

To control the motion of the movable wall by means of an electric field, it is required to charge this wall or produce a wall with an electric dipole moment. It has been hypothesized that the movable wall may be charged as a result of doping [18, 19]. According to calculations, the valence electron of an isolated potassium atom in the metallofullerene $K@C_{60}$ is completely transferred to fullerene C_{60} [83]. A similar charge transfer from metal atoms to a nanotube also takes place when metallofullerenes reside inside a single-walled nanotube [84]. Further charge transfer to the electrodes connected to the nanotube may occur in a nanoelectromechanical system based on such nanotubes. In this way, the metal atoms confined in the nanotube may become ions, and the internal wall containing the metal atoms may be set in motion with the help of an electric field [85]. The technology for the fabrication of these walls was proposed in Ref. [85]; it is based on the annealing of a nanotube with metallofullerenes inside of it and makes it possible to obtain only very short walls of uncontrollable length [86].

According to calculations, the electrostatic potentials at the open and capped ends of a SWNT are significantly different [87]. Consequently, if a wall is made open at one end and capped at the other, it would possess an electric dipole moment. Charge distribution simulations have revealed the emergence of a dipole moment in the chemical adsorption of Br_2 [88] and H_2O [89] molecules at the edge of a single-walled nanotube. Furthermore, the sign of the charge transferred to the edge depends on what atoms (donors or acceptors of electrons) are adsorbed at the open nanotube edges. We therefore suggest that the electric dipole moment of the wall be increased by way of adsorption of the donors and acceptors of charge at the opposite open edges of the wall. The motion of this wall may be controlled with the aid of a nonuniform electric field.

Electric dipole moments were calculated by the semiempirical molecular orbital method by the example of a 3.15-nm long SWNT (5,5) in two cases of chemical modification of the nanotube ends [90]. In the first case, one nanotube end was capped and electron donors were adsorbed at all dangling bonds of the open end. In the second case, both nanotube ends were open, with electron donors adsorbed at all dangling bonds of one end, and electron acceptors at all dangling bonds of the other end. Hydrogen and fluorine atoms were selected as the electron donors and acceptors, respectively. Our calculations showed that the electric dipole moments of the walls are equal to 4.536×10^{-29} C m in the former case, and 7.397×10^{-29} C m in the latter. The feasibility of controlling by means of a nonuniform electric field the motion of a NEMS based on a nanotube comprising walls-dipoles was demonstrated by the example of a gigahertz oscillator [90] (see Section 5.5).

5. Nanoelectromechanical systems reliant on the motion of nanotube walls

5.1 Nanobearings and nanomotors

The idea that MWNTs may be ideal nanobearings completely free from wear was put forward shortly after the discovery of nanotubes [91]. The energy dissipation during operation of DWNT-based nanobearings was simulated by the molecular dynamics method. By way of example, for nanobearings based on the DWNTs (9,9)@(14,14) and (9,9)@(22,4) with an interwall spacing of about 3.4 Å at a temperature of 300 K and an angular velocity of 3.1×10^{11} s^{-1}, the energy dissipation equals 3.3 and 3.7 meV per atom, respectively [92]. The energy dissipation rate was found to increase with temperature and to decrease with the spacing between the DWNT walls [13]. The spectra of the nanobearings exhibited low-frequency longitudinal, breathing, and torsional wall oscillations, medium-frequency oscillations which correspond to variations of the angles between the bonds, and high-frequency oscillations which correspond to variations of the bond lengths [13]. All these oscillations make contributions to the energy dissipation.

MWNT-based nanobearings have been used in recently fabricated nanomotors [26, 27]. In both nanomotors, a metal plate (the rotor) 200–500 nm in size was attached to the center of a movable MWNT wall secured between electrodes (Fig. 3). The control electrodes of the stator were arranged around the MWNT. The capacitance of this system, and hence the corresponding electrostatic energy, depends on the rotation angle of the plate attached to the outer MWNT wall. That is why the voltage applied across the plate and the stator electrodes produces an electrostatic torque which acts on the movable wall, thereby making it rotate.

In the former nanomotor realized, the plate was attached to the outer MWNT wall [26]. To open up the possibility of rotating this wall, a part of it in the region between the rotor electrodes and the plate was broken by applying an electrostatic force to the plate. In this nanomotor design, the inner walls make up the stator, and the outer wall serves as the rotor. To set the rotor in motion, the voltages $V_1 = V_0 \sin(\omega t)$, $V_2 = V_0 \sin(\omega t - \pi)$, $V_3 = V_0 \sin(2\omega t + \pi/2)$, and $V_r = -V_0$ were applied respectively to the three electrodes of the stator and to the rotor.

More recently, a nanomotor with improved design was made [26, 27]. In the fabrication of this motor, 5–10 outer MWNT walls in the middle of the region between the rotor electrodes were removed by ohmic heating. After that, the metal plane was attached to the middle of the outer remaining wall. In this nanomotor design, the inner walls make up the rotor, and the portions of the outer walls that survive at the nanotube ends serve as the stator. In this case, the caps of the outer walls (removed in the middle of the nanotube) hinder

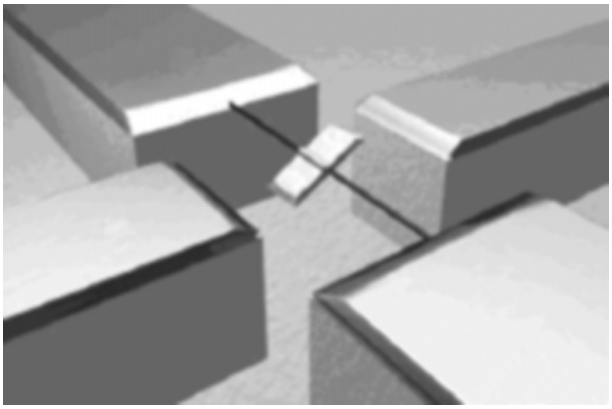

Figure 3. Schematics of a nanomotor reliant on the relative rotation of the walls of a carbon nanotube [26].

the displacement of the movable wall along the nanomotor axis.

5.2 Nanorelay and memory cell

A suggestion for a nanorelay based on the relative motion of carbon nanotube walls was recently put forward [16, 17]. Figure 4 shows several possible nanorelay schemes. In these nanorelays, a DWNT is attached to electrode *3*. The movable inner DWNT wall *1* telescopically extends from the outer wall *2* under the action of an electrostatic force F_e and is attracted to electrode *4* by the van der Waals force F_a due to the interaction between the inner wall and electrode *4* (turning the relay on). The inner wall is pulled back into the outer one by a van der Waals force F_W due to the interaction between the inner and outer walls (turning the relay off). The second electrode may be either metallic (Fig. 4a) [16] or a single-walled carbon nanotube (Fig. 4b) [17]. A nanorelay design with the third, control electrode made of a single-walled carbon nanotube has also been put forward (Fig. 4c) [17].

As indicated in Section 3, when the inner movable wall of the first electrode is nonchiral and commensurate with the outer wall, in the balance of forces that determine the nanorelay operation it is necessary also to take into account the static friction force F_f which impedes the relative motion of walls. The force F_f may be neglected for the relative motion of incommensurate and commensurate chiral wall pairs of the first electrode. The condition which permits the system to operate as a relay is bistability — the existence of two potential energy minima. An analysis of the balance of forces during the nanorelay operation shows that $F_a > F_W$ for the nanorelay with the second metallic electrode (Fig. 4a), and hence both potential energy minima exist in the absence of the control voltage [16, 17]. This nanorelay may be employed as an *nonvolatile memory cell* for any pair of walls of the first electrode. A memory device consisting of such cells is diagrammed in Fig. 4d. For a nanorelay based on the incommensurate DWNT (8,2)@(12,8) with the scheme shown in Fig. 4a, the turn-on and turn-off voltages (±3 V) and the switching time (10^{-11} s) were calculated, which corresponds to an operating frequency of 100 GHz [16].

A nanorelay in which both electrodes are made of carbon nanotubes offers several advantages over a nanorelay in which the second electrode is a metallic nanowire. The use of nanotubes as electrodes permits, first, decreasing the nanorelay dimensions and, second, attaining a higher evenness in dimensions and characteristics of the electrode surfaces. For a nanorelay with the second nanotube electrode, one obtains $F_a < F_W$. Consequently, for incommensurate and commensurate chiral wall pairs of the first electrode (in the absence of the friction force F_f), the nanorelay may stay in the 'on' position only when the control voltage is applied [17]. This nanorelay offers promise as a random-access memory (RAM) cell. According to estimates, for a nanorelay with the second and control electrodes made of nanotubes and having the smallest possible radii, the turn-on voltage and the voltage required for the retention in the 'on' state are equal to 6 and 4.8 V, respectively [17].

For a DWNT with commensurate nonchiral walls in which the friction force F_f is significant, it is possible to select the length of the outer wall so that the condition $F_a + F_f > F_W$ is fulfilled. In this case, the nanorelay with the nanotube second electrode may also be used as a read-only memory (ROM) cell. According to estimates, a nanorelay with the nanotube second electrode and the DWNT (5,5)@(10,10)-based first electrode may be bistable in the absence of control voltage when the wall overlap length l_{ov} of the DWNT (5,5)@(10,10) exceeds the critical value $l_c = 4$ nm [17]. However, the bistability condition $l_{ov} > l_c$ would not suffice for the adequate nanorelay operation as an energy-independent memory cell: the potential barrier ΔU which separates the 'on' and 'off' positions may be overcome due to the thermal diffusion of the inner wall. The probability p of such an event is defined by the Arrhenius formula $p = \Omega \exp(-\Delta U/kT)$, where Ω is the pre-exponential factor. According to simulations of the reorientation dynamics of the $C_{60}@C_{240}$ nanoparticle shells by the molecular dynamics method, the pre-exponential factor Ω exceeds the frequency of small oscillations about the equilibrium position by one order of magnitude [93, 94]. Figure 5 depicts the dependence of the 'on'-position lifetime $t = p^{-1}$ on the wall overlap length l_{ov}, calculated for a nanorelay with the nanotube second

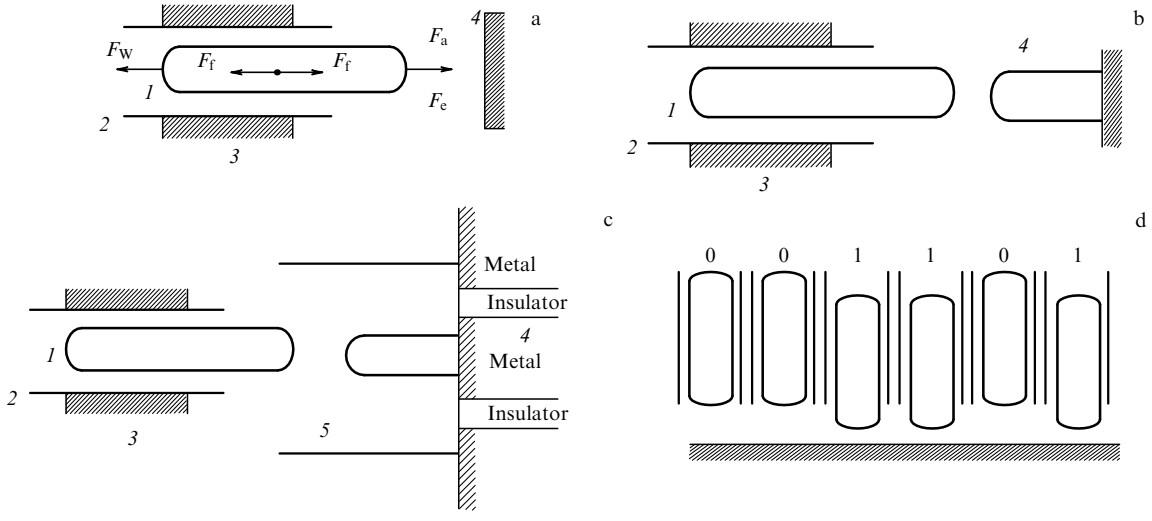

Figure 4. Schematics of DWNT-based electromechanical nanorelays (in the 'on' position): (a) a nanorelay with the second planar metallic electrode, (b) a nanorelay with a carbon nanotube as the second electrode, and (c) a nanorelay with a carbon nanotube as the control electrode: *1* — movable inner wall, *2* — fixed outer wall, *3* and *4* — electrodes. (d) Example of a storage made of DWNT-based memory cells.

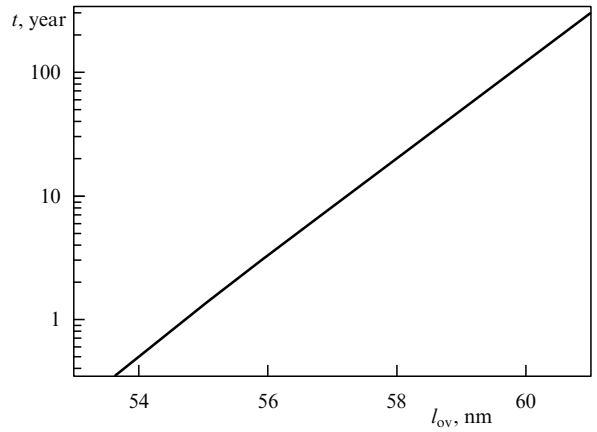

Figure 5. Dependence of the 'on'-position lifetime t on the wall overlap length l_{ov} at a temperature of 300 K, calculated for a nanorelay with the (5,5) nanotube second electrode and the DWNT (5,5)@(10,10)-based first electrode.

electrode and the DWNT (5,5)@(10,10)-based first electrode [17]. This plot demonstrates the feasibility of utilizing the nanorelay with the nanotube second electrode as a nonvolatile memory cell.

5.3 Nanoresistors

According to calculations, the conductivity of several carbon nanosystems, like a fullerene placed between two SWNTs [95] and a DWNT with telescopically extended walls [34–37], may alter by several orders of magnitude under relative displacements of the parts of a nanosystem by a distance of about 1 Å. We suggest that the relative displacements of the parts of both of these nanosystems and hence the nanoresistor conductivity be controlled with the aid of a DWNT-based nanoactuator [28–30]. In particular, advantage can be taken of a nanobolt–nanonut pair to transform an axially directed force into the rotation of the conducting wall or a torque-producing force into the axial sliding of this wall. The schematics of nanoresistors based on the above nanosystems are given in Fig. 6.

5.4 Electromechanical nanothermometer

We have come up with the conceptual idea of an electromechanical nanothermometer reliant on the interaction and relative motion of carbon nanotube walls, where the temperature is taken by measuring the conductivity [17, 39]. The relative position of the nanotube walls varies under temperature fluctuations as a result of relative thermal wall vibrations. The probability $p(z)$ of the relative displacement of the walls by a distance z along the nanotube axis depends on the interwall interaction energy $U(z)$ as $p(z) \sim \exp(-U(z)/kT)$. The total nanotube conductivity at a temperature T with the inclusion of thermal wall vibrations is defined by the following expression

$$G_{\text{tot}}(T) = \frac{\int_{-\infty}^{\infty} G(z,T)\,\exp\left(-U(z)/kT\right)\mathrm{d}z}{\int_{-\infty}^{\infty}\exp\left(-U(z)/kT\right)\mathrm{d}z}\,. \qquad (17)$$

The following conditions should be fulfilled for the operation of an electromechanical nanothermometer reliant on the interaction of carbon nanotube walls: $G(z,T)$ depends only slightly on the temperature for a fixed relative position of the walls (condition A); the conductivity $G(z,T)$ essentially depends on the z-coordinate which specifies the relative position of the walls (condition B); the characteristic amplitude of thermal wall vibrations is high enough for the thermal vibrations to make the main contribution to the temperature dependence of the conductivity (condition C) and is low enough for the relative wall displacements not to disrupt the nanothermometer operation (condition D).

Possible schemes of an electromechanical nanothermometer are depicted in Fig. 7. We considered the realizability of this nanothermometer by way of the example of a DWNT (6,6)@(11,11). The DWNT (6,6)@(11,11) conductivity depends essentially on the relative position of the walls for both nanothermometer schemes given in Fig. 7 [35]. Condition B is therefore fulfilled. Experimental data suggest that the conductivity of single-walled nanotubes possesses only a weak dependence on the temperature for $T > 50$ K [97]. Calculations show that the DWNT conductivity depends only slightly on the temperature for $T > 100$ K [39, 96]. Therefore, condition A is also fulfilled.

The dependences of the conductivity $G(z)$ and the interwall interaction energy $U(z)$ on the relative displacement z of the walls are defined by the symmetry of a DWNT (6,6)@(11,11). These dependences have common properties: their periods and extrema coincide. Furthermore, due to the incompatibility of wall rotation symmetries, both the conductivity and the interaction energy of the walls depend only slightly on the angle of relative wall rotation. Since adequate nanothermometer operation implies the absence of diffusive motion of the short wall relative to the long one, integration in formula (17) may be performed only in the vicinity of the minimum of the interwall interaction energy. In this domain, the dependence (7) of the interwall interaction energy on the relative wall position can be approximated by the expression

$$U(z') = U_1 + \frac{\pi\Delta U_z}{b^2}z'^2\,, \qquad (18)$$

where z' is the displacement of the movable wall with respect to the position corresponding to the minimum of the interwall interaction energy, and U_1 is the value of the wall interaction energy corresponding to the minimum. Since the extreme points of the dependences of the interwall interaction energy $U(z')$ and the conductivity $G(z')$ coincide, we approximated the dependence $G(z')$ for small displacements z' as follows:

$$G(z') = G_1(T)\,(1+\gamma z'^2)\,, \qquad (19)$$

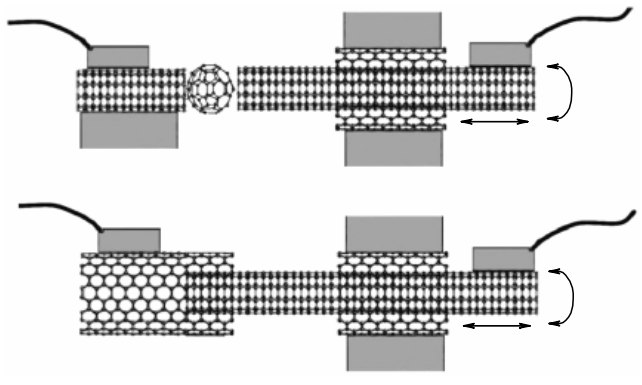

Figure 6. Basic diagrams of nanoresistors based on carbon nanotubes.

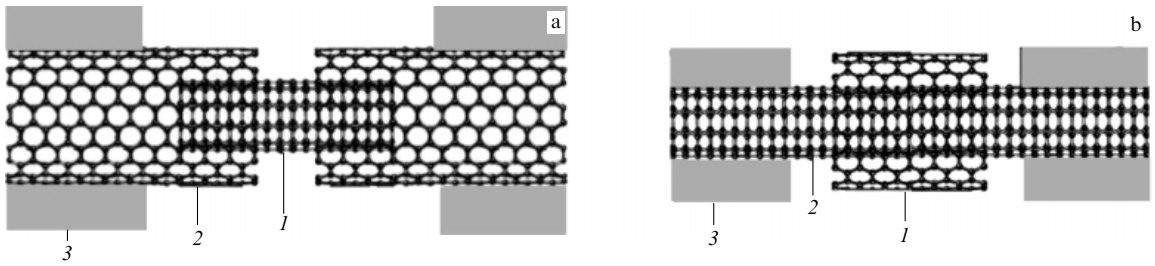

Figure 7. Schematics of electromechanical DWNT-based nanothermometers: (a) a telescopic nanothermometer with a movable inner wall, and (b) a nanothermometer with a movable shuttle from the outer wall: *1* — movable wall, *2* — fixed wall, and *3* — electrodes.

where G_1 is the conductivity value corresponding to the minimum of the interwall interaction energy. The γ-parameter value estimated from the dependence $G(z')$ given in Fig. 3 in Ref. [35] is $\gamma \sim 850$ Å^{-2} for a wall overlap of 2.45 nm and the nanothermometer scheme depicted in Fig. 7a.

On substituting expressions (18) and (19) into formula (17) we obtained the following relation for the temperature dependence of nanothermometer conductivity:

$$G(T) = G_1(T)\left(1 + \frac{\gamma b^2 kT}{\pi \Delta U_z}\right) = G_1(T)\,(1 + HT)\,. \quad (20)$$

According to the data calculated by the method of density functional, the barrier height is $\Delta U_z = 1.96$ eV for a wall overlap of 2.45 nm [12]. Therefore, $HT \approx 140$ for a temperature $T = 300$ K, which signifies the fulfillment of the condition C.

The condition D is fulfilled when the movable wall displacement d arising from diffusion turns out to be shorter than the movable wall – electrode spacing L_e:

$$d = \sqrt{2Dt} < L_e\,, \quad (21)$$

where D is the diffusion coefficient for the movable wall, and t is the nanothermometer operation time. The diffusion coefficients for the relative motion of DWNT walls were recently calculated with the help of the method of density functional [98]. By taking advantage of these data for the DWNT (6,6)@(11,11), we arrived at the conclusion that the interelectrode distance for a nanothermometer that would operate for 100 years without failure is equal to about 40 nm for both schemes depicted in Fig. 7. Therefore, the length of the proposed nanothermometer is actually determined by the length required to connect the electrodes to the nanotube, and it may be employed for nanolocal temperature measurements. The nanothermometer may be calibrated with the aid of a thermocouple, and it is possible to achieve the same measurement accuracy as for the thermocouple, since the nanothermometer relies on conductivity measurements (the accuracy of room-temperature measurements for copper – constantan and chromel – alumel thermocouples amounts to 0.1 K).

5.5 Gigahertz oscillator

On the basis of an MWNT it is possible to make a nanomechanical device in which there occurs a periodic motion at a very high frequency — on the order of 1 – 100 GHz [85, 78]. It has been suggested that these devices, which are termed gigahertz oscillators, be employed, in particular, in nanoactuators [18, 19]. The design and operation of the gigahertz oscillator are schematized in Fig. 8. The van der Waals force F_W, which retracts the telescopically extended inner wall into the outer one, essentially depends on the relative position of the walls only when the separation of the wall edges is on the order of the interwall distance. Therefore, in the standard theory of the gigahertz oscillator, the dependence of the force F_W on the distance x between the wall centers may be approximated by the following expression [18, 19]:

$$F_W(x) = \begin{cases} F_W, & |x| > |L - l|/2, \\ 0, & |x| < |L - l|/2, \\ 0, & |x| > |L + l|/2, \end{cases} \quad (22)$$

where L and l are the outer and inner wall lengths, respectively. For such an oscillator model, the dependence of the potential energy on the relative wall position is of the form given in Fig. 9. The natural frequency of small oscillations is absent from systems with such a potential, while the frequency of high-amplitude oscillations (which are targeted for use in NEMSs) depends strongly on the amplitude. That is why it is required to maintain a constant amplitude of these oscillations for the nanotube-based

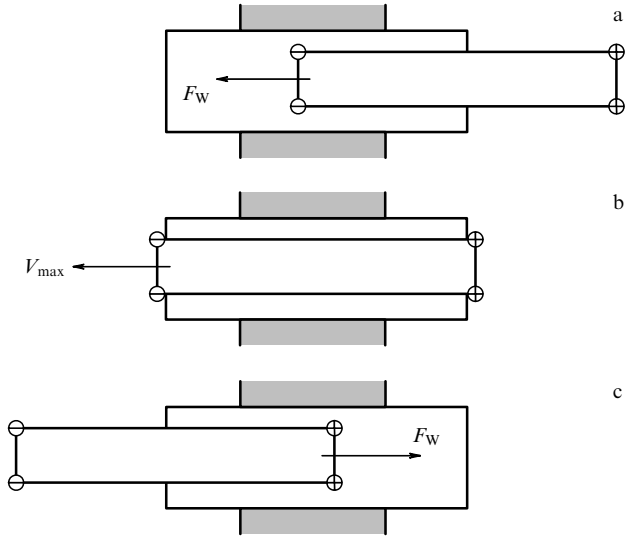

Figure 8. Sequential positions of the walls of a gigahertz oscillator during half the oscillation period: (a) and (c) the maximum telescopic extension of the inner wall; the van der Waals force F_W retracts the inner wall into the outer one; (b) moving under its own momentum, the inner wall passes at the highest velocity V_{max} through the position with the minimal potential energy.

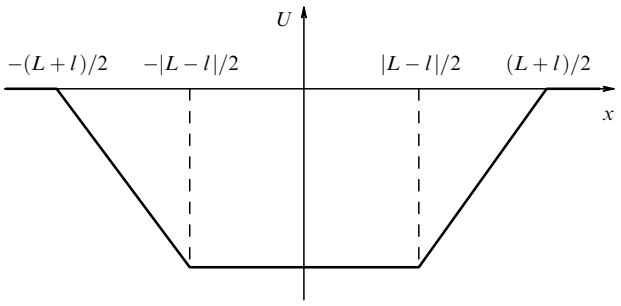

Figure 9. Schematic representation of the oscillator potential energy U as a function of the distance x between wall centers.

gigahertz oscillator frequency to remain invariable. The oscillation period T is defined by the expression

$$T = 2(t_{\text{in}} + t_{\text{out}}) = 2\left[(L - l) + 4s\right]\sqrt{\frac{m}{2F_{\text{W}}s}}, \tag{23}$$

where m is the inner wall mass, s is the maximum distance by which the inner wall extends from the outer one, $t_{\text{in}} = (L - l)\sqrt{m/2F_{\text{W}}s}$ is the time it takes for the inner wall to travel from one end of the outer wall to the other, and $t_{\text{out}} = 2\sqrt{2ms/F_{\text{W}}}$ is the time of an inner wall motion during which one of its ends is beyond the outer wall.

The characteristics of gigahertz oscillators were comprehensively studied by simulations using the molecular dynamics method [79, 99–106]. It was shown, in particular, that dynamic friction is responsible for oscillation energy dissipation: their free oscillations executed with a frequency which increases with time and decay in a time on the order of several nanoseconds [99, 100, 105] with a quality factor $Q = \Delta E/E \sim 100-1000$, where E and ΔE are the oscillator energy and the energy loss during one period [104, 105]. An analysis of the results of damped oscillation simulations revealed that the dependence of the dynamic friction force on the inner wall velocity V may be approximated as $F = -aV - b\,\text{sign}\,(V)\,V^2$ [106]. Then, during one period the friction force does the work

$$A_{\text{f}} = -2aV_{\text{max}}^2\left(\frac{t_{\text{out}}}{3} + t_{\text{in}}\right) - 2bV_{\text{max}}^3\left(\frac{t_{\text{out}}}{4} + t_{\text{in}}\right), \tag{24}$$

where $V_{\text{max}} = \sqrt{2F_{\text{W}}s/m}$ is the highest velocity of the inner wall [90].

The possibility of compensating for the energy dissipation was considered in the case when the motion of the inner oscillator wall is controlled by an external harmonic force $F(t) = F_0 \cos \omega t$ aligned with the wall axis, with ω corresponding to the desired oscillation frequency [90]. The work A_{c} of the force $F(t)$ in a period T is defined by the expression

$$A_{\text{c}} = \frac{4F_{\text{W}}F_0}{m\omega^2}\cos\left(\frac{\omega t_{\text{in}}}{2}\right), \tag{25}$$

where $\omega = 2\pi/T$ is the circular oscillation frequency. During the same time, the friction force does the work $A_{\text{f}} = -F_{\text{W}}s/Q$. From the condition $A_{\text{c}} + A_{\text{f}} = 0$, which signifies that the work of the controlling force compensates for the energy dissipation, we find the controlling force amplitude F_0:

$$F_0 = \frac{ms\omega^2}{4Q\cos(\omega t_{\text{in}}/2)}. \tag{26}$$

An analysis of expression (26) reveals that F_0 is minimal for the walls of equal length, $L = l$. In the case of equal wall lengths, the oscillation frequency is expressed as $\omega = (\pi/2)\sqrt{F_{\text{W}}/2ms}$, and relation (24) for the work done by the friction force takes on the form

$$A_{\text{f}} = -\frac{8a\sqrt{2F_{\text{W}}s}\,s}{3\sqrt{m}} - \frac{4bF_{\text{W}}s^2}{m}, \tag{27}$$

while expression (26) for the controlling force amplitude reduces to

$$F_0 = \frac{\pi^2 F_{\text{W}}}{32Q}. \tag{28}$$

The operating characteristics of a gigahertz oscillator were estimated by the example of an oscillator based on the DWNT (5,5)@(10,10) with equal wall lengths $L = l = 3.15$ nm (the frequency of oscillations with an amplitude $s = 1$ nm for this oscillator amounts to about 400 GHz). According to *ab initio* calculations, the interwall interaction energy in the DWNT (5,5)@(10,10) is 23.83 meV per atom of the outer wall [12], which corresponds to the value of $F_{\text{W}} = 625$ pN for the force drawing in the inner wall. For this value of the force F_{W} and a quality factor $Q = 1000$, the amplitude of controlling force reaches $F_0 = 0.193$ pN.

In particular, the harmonic controlling force may be applied to a wall-dipole with the aid of a nonuniform electric field. The calculated results for the dipole moments of walls-dipoles, given in Section 4.2, were used for estimating the voltage required to produce such a nonuniform electric field which would control the wall-dipole motion and maintain the stable oscillator frequency [90]. It was found that for a spherical capacitor with plates approximately 100 nm in diameter and a plate separation of about 10 nm it is possible to control the wall-dipole motion by applying the voltage $U(t) = U_0 \cos \omega t$ with the amplitudes $U_0 = 2.24$ and 2.77 V in the first and second cases of the walls-dipoles described in Section 4.2.

The master voltage was estimated for a nonuniform electric field produced by a charge distributed over the surface with a relatively weak curvature. Using the field produced by a charge on the surface with a stronger curvature, in particular, the field near a tip, would enable the control of a wall-dipole motion by applying a significantly lower voltage.

5.6 Nanoactuator

As indicated in Section 3, when the dependence of the interaction energy $U(\phi, z)$ of walls on their relative position possesses helical symmetry, the walls may be utilized as a nanobolt–nanonut pair. We suggest the use of this pair in a nanoactuator (Fig. 10) intended to transform into wall rotation the translational force aligned with the nanotube axis [17, 32, 33]. In such a nanoactuator, the stationary fixed nanotube wall *1* makes up the stator. Walls *1* and *2* are a rotation nanobearing, i.e., the condition $E_\phi \ll E_z$ is fulfilled for them, where E_ϕ and E_z are the potential barriers for the relative rotation of these walls and their relative sliding along the nanotube axis, respectively. This condition is fulfilled when walls *1* and *2* are nonchiral and commensurate [making a DWNT of the type $(n,n)@(m,m)$ or $(n,0)@(m,0)$]. For adequate nanoactuator operation it is desirable that the relative position of walls *2* and *3* be fixed. The relative

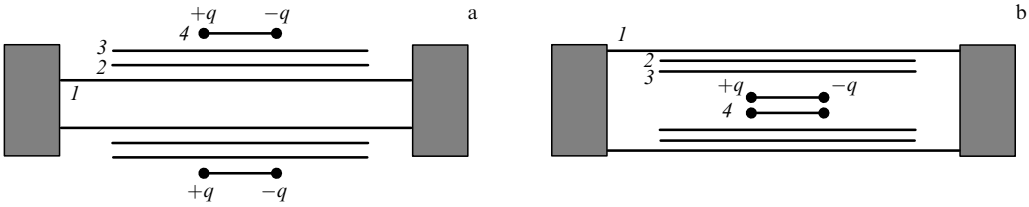

Figure 10. Schematics of a nanoactuator: (a) with the inner wall as the stator; (b) with the outer wall as the stator. Fixed wall *1* — the stator. Jointly rotating walls *2* and *3* — the rotor. Walls *3* and *4* make up a nanobolt – nanonut pair. The charges at the edges of wall *4* may be obtained by chemical adsorption and employed to control the nanoactuator with the aid of an electric field.

displacement of walls *2* and *3* along the nanotube axis will be prevented when wall *3* is nonchiral and commensurate with wall *2*. To avoid the relative rotation of walls *2* and *3* we suggest that atomic structural defects be made in wall *3*. The same defects periodically located at identical sites of the unit cells of wall *3* may be used to produce a nanobolt – nanonut pair from walls *3* and *4*. This pair serves to transform into rotor rotation the force applied to wall *4* and aligned with the nanotube axis.

Wall *4* will come into helical motion relative to wall *3* provided the following conditions are fulfilled: (i) the initial kinetic energy corresponding to the motion along the line of the thread is higher than the potential barrier E_1 for this motion:

$$\frac{M\mathbf{V}^2 \sin^2 \chi}{2} > E_1 \,, \tag{29}$$

where M and $\mathbf{F}$ are the mass and velocity of wall *4*, and χ is the thread angle; (ii) the initial kinetic energy corresponding to the motion across the line of the thread is lower than the potential barrier E_2 for twisting-off the thread:

$$\frac{M\mathbf{V}^2 \cos^2 \chi}{2} < E_2 \,. \tag{30}$$

It is easily shown that conditions (29) and (30) are simultaneously fulfilled only when

$$\cot^2 \chi < \frac{E_2}{E_1} = \beta \,. \tag{31}$$

Condition (31) assesses the feasibility of making a nanoactuator on the basis of a given nanobolt – nanonut pair. Note that it follows from condition (31) that nanobolt – nanonut pairs with a small relative depth of thread are suited for making a nanoactuator, when the thread angle exceeds 45°.

The conservation of the angular momentum of a nanoactuator determines the minimal rotor length L_3, whereby in the given nanoactuator it is possible to turn the rotor by an angle ξ:

$$L_3^{\min} = \frac{L_4^2 R_4^2}{L_4 R_4^2 + \xi (R_2^3 + R_3^3) \sin \chi} \,, \tag{32}$$

where L_4 is the length of wall *4*, and R_2, R_3, and R_4 are the respective radii of walls *2*, *3*, and *4*.

The complete list of four-walled nanotubes which may be employed in the making of this nanoactuator was given in Ref. [33]; also considered in Ref. [33] was a nanoactuator based on the (11,2)@(12,12)@(19,19)@(26,26) nanotube. The (11,2)@(12,12) nanobolt – nanonut pair, which makes up the inner walls in this nanoactuator, has a rather large relative depth of thread: $\beta = 5.812$. Furthermore, condition (31) is fulfilled for any relative depth of thread for a thread angle $\chi = 70.9°$ calculated for this nanobolt – nanonut pair.

6. Summary

In conclusion, let us list the results achieved in the development of nanotechnology techniques required for the fabrication of nanotube-based nanoelectromechanical systems. At the present time, with the help of a nanomanipulator it is possible to transfer SWNTs [107, 108] and set the walls of multi-walled nanotubes in relative motion [5]. Also effected was the removal of caps which covered the ends of nanotubes [109 – 111] and cutting nanotube walls into parts of desired lengths [112]. Several nanoelectromechanical systems considered in our report, in particular, a nanothermometer and a nanoactuator, can be made only of walls with specific chirality indices. In this connection, we note that a technique has been devised recently for the unambiguous determination of wall chirality indices [113].

The majority of the nanoelectromechanical systems that were the concern of our report were considered by way of the example of double-walled nanotubes. These nanotubes may be obtained by different synthesis techniques: in a conventional arc for the production of carbon nanotubes [7, 114], in the same arc in the presence of hydrogen and a catalyst [115, 116], and in the catalytic decomposition of hydrocarbons [117 – 123], as well as by heating [86, 124, 125] or electron irradiation [126] of single-walled nanotubes containing a fullerene chain inside.

Therefore, great progress in nanotechnology gives us hope that the carbon nanotube-based nanoelectromechanical systems considered in our report may be fabricated in the near future.

This work was supported by the Russian Foundation for Basic Research (grants Nos 06-02-81036-Bel-a and 05-02-17864-a).

References

1. Junno T et al. *Appl. Phys. Lett.* **66** 3627 (1995)
2. Porto M, Urbakh M, Klafter J *Phys. Rev. Lett.* **84** 6058 (2000)
3. Yu M-F et al. *Science* **287** 637 (2000)
4. Yu M-F, Yakobson B I, Ruoff R S *J. Phys. Chem. B* **104** 8764 (2000)
5. Cumings J, Zettl A *Science* **289** 602 (2000)
6. Kis A et al. *Phys. Rev. Lett.* **97** 025501 (2006)
7. Iijima S *Nature* **354** 56 (1991)
8. Treacy M M J, Ebbesen T W, Gibson J M *Nature* **381** 678 (1996)
9. Wong E W, Sheehan P E, Lieber C M *Science* **277** 1971 (1997)

10. Krishnan A et al. *Phys. Rev. B* **58** 14013 (1998)
11. Poncharal P et al. *Science* **283** 1513 (1999)
12. Bichoutskaia E et al. *Phys. Rev. B* **73** 045435 (2006)
13. Tuzun R E, Noid D W, Sumpter B G *Nanotechnology* **6** 64 (1995)
14. Srivastava D *Nanotechnology* **8** 186 (1997)
15. Forró L *Science* **289** 560 (2000)
16. Maslov L *Nanotechnology* **17** 2475 (2006)
17. Popov A M et al. *Phys. Status Solidi A* **204** 1911 (2007)
18. Zheng Q, Jiang Q *Phys. Rev. Lett.* **88** 045503 (2002)
19. Zheng Q, Liu J Z, Jiang Q *Phys. Rev. B* **65** 245409 (2002)
20. Tu Z C, Ou-Yang Z C *J. Phys.: Condens. Matter* **16** 1287 (2004)
21. Tu Z C, Hu X *Phys. Rev. B* **72** 033404 (2005)
22. Saito R et al. *Appl. Phys. Lett.* **60** 2204 (1992)
23. Tans S J, Verschueren A R M, Dekker C *Nature* **393** 49 (1998)
24. Tamura R *Phys. Rev. B* **64** 201404(R) (2001)
25. Menon M et al. *Phys. Rev. Lett.* **91** 145501 (2003)
26. Fennimore A M et al. *Nature* **424** 408 (2003)
27. Bourlon B et al. *Nano Lett.* **4** 709 (2004)
28. Lozovik Yu E, Minogin A V, Popov A M *Phys. Lett. A* **313** 112 (2003)
29. Lozovik Yu E, Minogin A V, Popov A M *Pis'ma Zh. Eksp. Teor. Fiz.* **77** 759 (2003) [*JETP Lett.* **77** 631 (2003)]
30. Lozovik Yu E, Popov A M *Fullerenes, Nanotubes Carbon Nanostruct.* **12** 463 (2004)
31. Saito R et al. *Chem. Phys. Lett.* **348** 187 (2001)
32. Lozovik Yu E, Nikolaev A G, Popov A M *Zh. Eksp. Teor. Fiz.***130** 516 (2006) [*JETP* **103** 449 (2006)]
33. Kuznetsov S S, Lozovik Yu E, Popov A M *Fiz. Tverd. Tela* **49** 951 (2007) [*Phys. Solid State* **49** 1004 (2007)]
34. Hansson A, Stafström S *Phys. Rev. B* **67** 075406 (2003)
35. Grace I M, Bailey S W, Lambert C J *Phys. Rev. B* **70** 153405 (2004)
36. Tunney M A, Cooper N R *Phys. Rev. B* **74** 075406 (2006)
37. Kim D-H, Chang K J *Phys. Rev. B* **66** 155402 (2002)
38. Bichoutskaia E et al. *Fullerenes, Nanotubes Carbon Nanostruct.* **14** 131 (2006)
39. Bichoutskaia E et al. *Phys. Lett. A* **366** 480 (2007)
40. Sazonova V et al. *Nature* **431** 284 (2004)
41. Kim P, Lieber C M *Science* **286** 2148 (1999)
42. Akita S et al. *Appl. Phys. Lett.* **79** 1691 (2001)
43. Rueckes T et al. *Science* **289** 94 (2000)
44. Jishi R A, Dresselhaus M S, Dresselhaus G *Phys. Rev. B* **47** 16671 (1993)
45. Iijima S, Ichihashi T *Nature* **363** 603 (1993)
46. Bethune D S et al. *Nature* **363** 605 (1993)
47. Zhang X B et al. *Europhys. Lett.* **27** 141 (1994)
48. Delhaes P (Ed.) *World of Carbon* Vol. 1 *Graphite and Precursors* (Amsterdam: Gordon and Breach, 2001)
49. Srivastava D, Wei C, Cho K *Appl. Mech. Rev.* **56** 215 (2003)
50. Tombler T W et al. *Nature* **405** 769 (2000)
51. Salvetat J-P et al. *Phys Rev. Lett.* **82** 944 (1999)
52. Yu M-F et al. *Phys. Rev. Lett.* **84** 5552 (2000)
53. Van Lier G et al. *Chem. Phys. Lett.* **326** 181 (2000)
54. Hernández E et al. *Phys. Rev. Lett.* **80** 4502 (1998)
55. Hernández E et al. *Appl. Phys. A* **68** 287 (1999)
56. Sánchez-Portal D et al. *Phys. Rev. B* **59** 12678 (1999)
57. Mielke S L et al. *Chem. Phys. Lett.* **390** 413 (2004)
58. Popov V N, Van Doren V E, Balkanski M *Phys. Rev. B* **61** 3078 (2000)
59. Lu J P *Phys. Rev. Lett.* **79** 1297 (1997)
60. Li C, Chou T-W *Int. J. Solids Struct.* **40** 2487 (2003)
61. Shen L, Li J *Phys. Rev. B* **69** 045414 (2004)
62. Benedict L X et al. *Chem. Phys. Lett.* **286** 490 (1998)
63. Bichoutskaia E et al. *Phys. Rev. B* **71** 113403 (2005)
64. Giessibl F J *Rev. Mod. Phys.* **75** 949 (2003)
65. Soule D E, Nezbeda C W *J. Appl. Phys.* **39** 5122 (1968)
66. Lozovik Yu E, Popov A M, Belikov A V *Fiz. Tverd. Tela* **45** 1333 (2003) [*Phys. Solid State* **45** 1396 (2003)]
67. Belikov A V et al. *Chem. Phys. Lett.* **385** 72 (2004)
68. Damnjanović M et al. *Phys. Rev. B* **60** 2728 (1999)
69. Damnjanović M et al. *New J. Phys.* **5** 148 (2003)
70. Damnjanović M, Vuković T, Milošević I *Eur. Phys. J. B* **25** 131 (2002)
71. Vuković T, Damnjanović M, Milošević I *Physica E* **16** 259 (2003)
72. Charlier J-C, Michenaud J-P *Phys. Rev. Lett.* **70** 1858 (1993)
73. Palser A H R *Phys. Chem. Chem. Phys.* **1** 4459 (1999)
74. Kolmogorov A N, Crespi V H *Phys. Rev. Lett.* **85** 4727 (2000)
75. White C T, Robertson D H, Mintmire J W *Phys. Rev. B* **47** 5485 (1993)
76. Lozovik Yu E, Nikolaev A G, Popov A M *Int. J. Nanotechnol.* **2** 255 (2005)
77. Belikov A V et al. *Fullerenes, Nanotubes Carbon Nanostruct.* **12** 117 (2004)
78. Kang J W et al. *Nanotechnology* **16** 2670 (2005)
79. Legoas S B et al. *Nanotechnology* **15** S184 (2004)
80. Tsang S C et al. *Nature* **372** 159 (1994)
81. Zhang G L et al. *J. Appl. Phys.* **80** 579 (1996)
82. Demoncy N et al. *Eur. Phys. J. B* **4** 147 (1998)
83. Li Y S, Tománek D *Chem. Phys. Lett.* **221** 453 (1994)
84. Kwon Y-K, Tománek D, Iijima S *Phys. Rev. Lett.* **82** 1470 (1999)
85. Kang J W, Hwang H J *J. Appl. Phys.* **96** 3900 (2004)
86. Bandow S et al. *Chem. Phys. Lett.* **337** 48 (2001)
87. Peralta-Inga Z et al. *Nano Lett.* **3** 21 (2003)
88. Park N et al. *Chem. Phys. Lett.* **403** 135 (2005)
89. Hwang Y G, Lee Y H *J. Korean Phys. Soc.* **42** S267 (2005)
90. Ershova O V et al. *Fiz. Tverd. Tela* **49** 1914 (2007) [*Phys. Solid State* **49** 2010 (2007)]
91. Drexler K E *Nanosystems: Molecular Machinery, Manufacturing, and Computation* (New York: Wiley, 1992) p. 297
92. Zhang S, Liu W K, Ruoff R S *Nano Lett.* **4** 293 (2004)
93. Lozovik Yu E, Popov A M *Chem. Phys. Lett.* **328** 355 (2000)
94. Lozovik Yu E, Popov A M *Fiz. Tverd. Tela* **44** 180 (2002) [*Phys. Solid State* **44** 186 (2002)]
95. Guttierrez R et al. *Phys. Rev. B* **65** 113410 (2002)
96. Ivanchenko G S, Lebedev N G *Fiz. Tverd. Tela* **49** 183 (2007) [*Phys. Solid State* **49** 189 (2007)]
97. Gao B et al. *Phys. Rev. Lett.* **95** 196802 (2005)
98. Bichoutskaia E et al. *Fullerenes, Nanotubes Carbon Nanostruct.* **14** 215 (2006)
99. Rivera J L, McCabe C, Cummings P T *Nano Lett.* **3** 1001 (2003)
100. Rivera J L, McCabe C, Cummings P T *Nanotechnology* **16** 186 (2005)
101. Legoas S B et al. *Phys. Rev. Lett.* **90** 055504 (2003)
102. Guo W et al. *Phys. Rev. Lett.* **91** 125501 (2003)
103. Servantie J, Gaspard P *Phys. Rev. Lett.* **91** 185503 (2003)
104. Zhao Y et al. *Phys. Rev. Lett.* **91** 175504 (2003)
105. Ma C-C et al. *Nanotechnology* **16** 1253 (2005)
106. Tangney P, Louie S G, Cohen M L *Phys. Rev. Lett.* **93** 065503 (2004)
107. Yu M et al. *Nanotechnology* **10** 244 (1999)
108. Shen Z et al. *Int. J. Nanosci.* **1** 575 (2002)
109. Tsang S C, Harris P J F, Green M L H *Nature* **362** 520 (1993)
110. Ajayan P M et al. *Nature* **362** 522 (1993)
111. Liu J et al. *Science* **280** 1253 (1998)
112. El-Hami K, Matsushige K *Int. J. Nanosci.* **2** 125 (2003)
113. Liu Z, Qin L-C *Chem. Phys. Lett.* **408** 75 (2005)
114. Ebbesen T W, Ajayan P M *Nature* **358** 220 (1992)
115. Hutchison J L et al. *Carbon* **39** 761 (2001)
116. Saito Y, Nakahira T, Uemura S *J. Phys. Chem. B* **107** 931 (2003)
117. Flahaut E et al. *J. Mater. Chem.* **10** 249 (2000)
118. Zhu H et al. *Carbon* **40** 2023 (2002)
119. Ren W et al. *Chem. Phys. Lett.* **359** 196 (2002)
120. Li W Z et al. *Chem. Phys. Lett.* **368** 299 (2003)
121. Ci L et al. *Chem. Phys. Lett.* **359** 63 (2002)
122. Wei J et al. *Chem. Phys. Lett.* **376** 753 (2003)
123. Zhu J, Yudasaka M, Iijima S *Chem. Phys. Lett.* **380** 496 (2003)
124. Smith B W, Luzzi D E *Chem. Phys. Lett.* **321** 169 (2000)
125. Abe M et al. *Phys. Rev. B* **68** 041405 (2003)
126. Sloan J et al. *Chem. Phys. Lett.* **316** 191 (2000)